Specific synaptic input strengths determine the computational properties of excitation - inhibition integration in a sound localization circuit

Enida Gjoni[1], Friedemann Zenke[2, 3] , Brice Bouhours[1], Ralf Schneggenburger[1*]

[1] Laboratory of Synaptic Mechanisms, Brain Mind Institute, School of Life Science, École Polytechnique Fédérale de Lausanne (EPFL), 1015 Lausanne, Switzerland
[2] Laboratory of Computational Neuroscience, Brain Mind Institute, School of Life Science and School of Computer and Communication Sciences, École Polytechnique Fédérale de Lausanne (EPFL), 1015 Lausanne, Switzerland
[3] Centre for Neural Circuits and Behaviour, Department of Physiology, Anatomy and Genetics, University of Oxford.

* corresponding author (ralf.schneggenburger@epfl.ch)

Running title: E - I integration in a binaural auditory nucleus

50 pages, 7 Figures, 0 Tables

Word count: Key Points: 146 words; Abstract: 250 words; Introduction: 732 words; Discussion: 2367 words

Key points

- During the computation of sound localization, neurons of the Lateral Superior Olive (LSO) integrate synaptic excitation arising from the ipsilateral ear with inhibition from the contralateral ear.
- We characterized the functional connectivity of the inhibitory and excitatory inputs onto LSO neurons in terms of unitary synaptic strength and convergence.
- Unitary inhibitory postsynaptic currents (IPSCs) can generate large conductances but their strength varies over a 10- fold range in a given recording. On the contrary, excitatory inputs are relatively weak.
- The conductance associated with IPSPs needs to be at least 2-fold stronger than the excitatory one to guarantee effective inhibition of action potential (AP) firing.
- Computational modeling showed that strong unitary inhibition ensures an appropriate slope and midpoint of the tuning curve of LSO neurons, while weak but numerous excitatory inputs filter out spontaneous AP firing from upstream auditory neurons.

Abstract

The lateral superior olive (LSO) is a binaural nucleus in the auditory brainstem in which excitation from the ipsilateral ear is integrated with inhibition from the contralateral ear. It is unknown whether the strength of the unitary inhibitory- and excitatory inputs is adapted to allow for optimal tuning curves of LSO neuron action potential (AP) firing. Using electrical and optogenetic stimulation of afferent synapses, we found that the strength of unitary inhibitory inputs to a given LSO neuron can vary over a ~ 10-fold range; follows a roughly log-normal distribution, and on average causes a large conductance (9 nS). Conversely, unitary excitatory inputs, stimulated optogenetically under the bushy-cell specific promoter Math5 were numerous, and each caused a small conductance change (0.7 nS). About 5 - 7 bushy cell inputs had to be active simultaneously to bring an LSO neuron to fire. In double stimulation experiments, the effective inhibition window caused by IPSPs was short (1 - 3 ms) and its length depended on the inhibitory conductance; an about 2 - fold stronger inhibition than excitation was needed to suppress AP firing. Computational modeling suggests that few, but strong unitary IPSPs create a tuning curve of LSO neuron firing with appropriate slope and midpoint, while weak but numerous excitatory inputs reduce the spontaneous AP firing that LSO neurons would otherwise inherit from their upstream auditory neurons. Thus, the specific connectivity, and strength of unitary excitatory and inhibitory inputs to LSO neurons is optimized for the computations performed by these binaural neurons.

Introduction

The superior olivary complex in the auditory brainstem computes the localization of sounds, and contains binaural nuclei like the LSO and the medial superior olive (MSO), which receive inputs from both ears (Masterton *et al.*, 1967; Tollin, 2003; Grothe *et al.*, 2010). The LSO receives inhibitory input from the medial nucleus of the trapezoid body (MNTB), which informs LSO neurons about a tone at the contralateral ear (Sanes, 1990; Kim & Kandler, 2003). LSO neurons also receive excitatory input from the *ipsilateral* cochlear nucleus, most probably originating from bushy cells (Spirou *et al.*, 1990; Smith *et al.*, 1991; Smith *et al.*, 1993; Saul *et al.*, 2008; see Cant & Benson, 2003 for a review). These synaptic inputs to LSO neurons thus explain the classical findings from *in-vivo* recordings showing that LSO neurons are *excited* by ipsilateral sounds, but inhibited by contralateral sounds (Boudreau & Tsuchitani, 1968; Magnusson *et al.*, 2008; Karcz *et al.*, 2011; for review, see Tollin, 2003; Grothe *et al.*, 2010).

The MNTB - LSO inhibitory synapse has previously been studied *in-vitro* as a model for a developing inhibitory synapse in the auditory brainstem. Thus, it was shown that the MNTB - LSO connection has GABAergic and glutamatergic components early in development, and that it changes to a purely glycinergic connection after hearing onset (Kotak *et al.*, 1998; Gillespie *et al.*, 2005). Furthermore, IPSC amplitudes increase with development at around the same time, and separate unitary IPSCs are observed in electrical fiber stimulation experiments from ~ postnatal day (P) 9 onwards (Kim & Kandler, 2003; Walcher *et al.*, 2011). The excitatory inputs to LSO neurons show a rather graded input - output relation (Case & Gillespie, 2011; Xiao *et al.*, 2013), although some evidence for a developmental refinement towards larger unitary excitatory postsynaptic currents (EPSCs) was recently found (Case & Gillespie, 2011; Felix & Magnusson, 2016). Thus, it seems that LSO neurons receive a multitude of small excitatory synaptic inputs, unlike for example the specialized large 1:1 calyx of Held synapse between globular bushy cells and MNTB neurons (Schneggenburger & Forsythe, 2006; Borst & Soria van Hoeve, 2012). Nevertheless, the advantages of a graded excitatory input to LSO neurons, and of relatively large unitary inhibitory inputs for the excitation – inhibition (E-I) integration performed by the LSO neurons, have not been investigated.

Many of the previous studies of inhibitory- and excitatory synaptic inputs to LSO neurons have been performed with fiber stimulation experiments. An alternative method to stimulate genetically defined synaptic afferents is optogenetic stimulation (Boyden *et al.*, 2005). Here, the expression of a light-activated ion channel like Channelrhopsin-2 (ChR2) can be targeted with Cre-lox systems to molecularly defined neuron populations (Madisen *et al.*, 2012). Optic stimulation of ChR2-expressing afferent fibers can then be used to evoke synaptic currents of molecularly defined origin (Petreanu *et al.*, 2007). Here, we have made use of such optogenetic stimulation techniques to investigate E-I integration in LSO neurons.

At the outset of our study, using electrical fiber stimulation in young hearing mice, we found that unitary IPSCs were larger, and had a larger variability across separate inputs than reported previously (Kim & Kandler, 2003, 2010; Noh *et al.*, 2010; Hirtz *et al.*, 2012; but see Walcher *et* *al.*, 2011). This prompted us to investigate the amplitude of unitary IPSCs also with optogenetic stimulation, which revealed unusually strong compound IPSCs after near-maximal optogenetic stimulation, and large, but variable unitary IPSCs. In a parallel study, we reconstructed the inhibitory axons that make contact with the soma and proximal dendrite of an LSO neuron using serial block face electron microscopy (SBEM; Denk & Horstmann, 2004). We found that an LSO neuron is densely surrounded by a multitude of inhibitory axons which together contain at least 300 active zones, a finding which provides the ultrastructural correlate for strong inhibition of LSO neurons (Gjoni et al., *accompanying manuscript*). In strong contrast to inhibition, optogenetic stimulation of excitatory fibers from bushy cells in the VCN produced graded EPSCs with small unitary EPSC amplitudes. Modelling approaches suggested that this distribution of the strengths of unitary postsynaptic currents (PSC) and the degree of convergence observed for both inhibition and excitation, determines the steepness of the tuning curve of AP-firing of LSO neurons and the spontaneous AP firing of LSO neurons. Thus, the specific connectivity of excitatory - and inhibitory inputs to LSO neurons is optimized for the E - I integration process performed by these binaural neurons.

Methods

Ethical Approval

All procedures with research animals (mus musculus; different transgenic strains see below) were approved by the veterinary office of the Canton of Vaud, Switzerland (authorization # 2063.3, 2063.4), and conform to the Journal of Physiology’s guideline on animal ethics. Research work at our institution operates under the Swiss Federal law on the protection of animals ("Loi fédérale sur la protection des animaux"). Mouse pups were housed in standard cages with their mother, under ad libitum access to food and water under a 12h/12h dark/light cycle. On the day of the experiment, a mouse pup was sacrificed by decapitation prior to making native brain slices, in a procedure approved by the veterinary office of the Canton of Vaud, Switzerland (authorization # 2063.3, 2063.4).

Animals

Most experiments were done with mouse pups at postnatal days (P) 16 - 21. Two additional preparations were done with adult mice (P40 and P68; data not shown). For the optogenetic stimulation experiments (Figs 3-6), a Cre-dependent Channelrhodopsin (H134R) - eYFP reporter mouse line (abbreviated *ChR2*; RRID:IMSR_JAX:012569; Madisen *et al.*, 2012), was crossed with one of the below *Cre*-mouse lines, depending on the purpose of the experiment. A *Parvalbumin-IRES*-Cre line (abbreviated PV^{Cre} ; RRID:IMSR_JAX:017320; Hippenmeyer *et al.*, 2005) was used for the experiments in Figs 3 and 4 to stimulate inhibitory- and excitatory inputs, respectively. In order to stimulate bushy cell inputs more specifically (Figs 5, 6), the *ChR2* mice were crossed with a $Math5^{Cre}$ mouse line kindly provided by Dr. Lin Gan (Yang *et al.*, 2003). For the latter breeding pairs, typically only one parent had a $Math5^{Cre}$ allele, to avoid generating $Math5^{Cre/Cre}$ (*Math5* null) mice (Yang *et al.*, 2003). For the former breedings, mice heterozygous for the PV^{Cre} allele were used. For *ChR2* mice, either heterozygous or homozygous mice were used as breeders. For all other experiments, C57Bl6/J mice were used. Mice of either sex were used, but the sex of the mice was in most cases not determined.

Slice preparation and electrophysiology

Coronal 200 µm slices of the mouse brainstem containing MNTB and LSO were cut using a Leica VT1000S slicer (Leica Microsystems, Wetzlar, Germany) according to standard procedures (von Gersdorff *et al.*, 1997). For optogenetic stimulation of inhibitory neurons in the MNTB (Fig. 3I-L), slice thickness was 300 µm and the slice angle was slightly tilted medio-laterally (~ 15°) to improve the preservation of fibers from MNTB to LSO. During dissection of the brainstem and the slicing procedure, the tissue was submerged in ice-cold solution containing (in mM): 125 NaCl, 25 $NaHCO_3$, 2.5 KCl, 1.25 NaH_2PO_4, 25 Glucose, 0.4 ascorbic acid, 3 myo-inositol and 2 Na-pyruvate, supplemented with 0.1 $CaCl_2$ and 3 $MgCl_2$ (all from Sigma-Aldrich/Fluka, Buchs, Switzerland), bubbled with 95% O_2, 5% CO_2 (pH 7.4). The slices were transferred to a submerged incubation chamber with standard bicarbonate-based solution as above, but containing 2 mM $CaCl_2$ and 1 mM $MgCl_2$, and were kept there for at least 45 min at 35°C before the recordings. We made recordings in the medial limb of the LSO, and targeted LSO neurons with relatively large somata. The recorded neurons had a baseline cell capacitance of 12 - 15 pF and thus likely represent the larger principal neurons as opposed to neurons of the lateral olivocochlear bundle which have smaller somata (Sterenborg *et al.*, 2010). Whole-cell patch-clamp recordings were done at room temperature (22 - 24°C), using an EPC10/2 patch-clamp amplifier (HEKA Elektronik, Lambrecht/Pfalz, Germany).

For measurements of IPSCs under conditions of high intracellular Cl^- ion concentration ($[Cl^-]_i$) (Figs 1, 3), the patch pipette solution contained (in mM): 140 CsCl, 10 HEPES, 20 TEA-Cl, 5 Na_2-phosphocreatine, 4 Mg-ATP, 0.3 Na_2-GTP, 0.2 EGTA (pH 7.2 with CsOH), with a total $[Cl^-]_i$ of 160 mM. In these experiments, IPSCs were measured at a holding potential (V_h) of -70 mV, initially with 10 µM NBQX and 50µM APV (Biotrend, Wangen, Switzerland) in the extracellular solution to block excitatory synaptic currents. However, because NBQX at high concentrations is an antagonist of homomeric glycine receptors, we later switched to 10 µM CNQX which has significantly lower potency at glycine receptors (Meier & Schmieden, 2003). We estimate that the unitary IPSCs reported for some recordings in Fig. 1 might have been underestimated by ~ 30% because of the blocking effect of NBQX on glycine receptors.

The experiments of Figs. 2, 5 and 6 were performed with a patch-pipette solution with "low" $[Cl^-]_i$, containing (in mM): 145 K-gluconate, 6 KCl, 10 HEPES, 3 Na_2-phosphocreatine, 4 Mg-ATP, 0.3 Na_2-GTP, 0.2 EGTA; pH 7.2 with KOH. The total $[Cl^-]$ was 6 mM, close to a previous estimate of intracellular [Cl^-] in LSO neurons of near-mature rats (Ehrlich *et al.*, 1999). Considering the extracellular [Cl^-] of 133 mM and a temperature of 22°, we calculate the Cl^- equilibrium potential to be -78.8 mV and +4.6 mV for low - and high [Cl^-]$_i$ conditions, respectively. In the voltage-clamp experiments under low [Cl^-]$_i$, the IPSCs were recorded at a V_h of -50 mV (Fig. 2). Membrane potential values were not corrected for liquid junction potential. For the recordings of EPSCs in Fig. 4, the Cs-based intracellular solution with high [Cl^-]$_i$ was used (see above).

The series resistance (R_s) was in the range of 4 to 10 MOhm, exceptionally up to 15 MOhm, and was compensated by 50 - 90 % by the patch-clamp amplifier. All displayed, and analyzed IPSC- and EPSC traces were corrected for the remaining R_s error in an off-line analysis procedure (Meyer *et al.*, 2001; see also Fig. 1A3). If the correction increased the peak IPSC by more than 50 %, the data was discarded. Recordings were made using the lowest possible gain (0.5 mV/pA) with the intermediate feedback resistor of the EPC-10 (500 MOhm). With these setting, currents of up to +/- 20 nA amplitude can be recorded, before amplifier saturation occurs. However, considering R_s-errors, we estimate that the true currents close to saturation of the amplifier correspond to ~ 30 nA (see above). In some recordings with strong optogenetic stimuli, V_h was set to -20mV to avoid amplifier saturation (Fig. 3C2).

Electrical fiber-stimulation was performed with a custom-built platinum/iridium bipolar electrode, which was placed medially to the LSO for activating fibers originating from MNTB (Figs. 1, 2 and 6). Short pulses (0.1 ms) were delivered via an isolated stimulator (A-M Systems, Model 2100, Carlsborg, WA, USA). To measure IPSC amplitudes as a function of stimulus intensity (input-output curves; e.g. Figs. 1A, B) we applied n = 8 stimuli at 0.1 Hz at a given stimulus intensity. We attempted to map out the recruitment of new fibers with finer stimulation increments, but used larger increments when no additional fibers appeared; thus, the stimulation increments were not constant.

Optical stimulation

For optogenetic stimulation (Figs. 3 - 6), blue light pulses were generated by a LED controller (Doric lenses, Québec, Canada) driving a high-power LED (CREE XP-E2 Royal Blue, 450-460 nm; Cree Inc, NC, USA). The light was coupled into the microscope (ZEISS, Axioskop 2, FS plus) using an epifluorescence condenser (TILL photonics, Planegg, Germany) and focused onto the sample with a 40x objective (Olympus LUM Plan FL, 0.8 NA). The light output was restricted to an area of ~160 x 120 µm with an aperture; during most experiments the recorded LSO neuron was positioned in the middle of the illuminated area. In the experiments of Fig. 3I-L, after establishing a recording of an LSO neuron, the microscope optical axis was carefully moved to the MNTB by means of an x-y table mounted below the microscope, to allow optical stimulation of groups of MNTB neurons.

In the majority of the experiments, the light intensity was modulated with neutral density (ND) filters (5%, 10%, 25% and 50%, alone or in combination), while using only the upper half of possible voltage ranges fed into the LED controller (range 2.5 - 5 V). This is because voltage pulses below 2 V led to timing errors of the LED controller (Doric lenses). The time course of light pulses was measured with a photodiode (DET36A/M, ThorLabs, USA); stimulus light intensity is expressed as percent of the maximal light intensity (5 V at the LED controller and no ND filter corresponding to "100 %").

Analysis of electrophysiological data

During offline-analysis, IPSC and EPSC traces were first corrected for the remaining R_s error (see above). In the plots of peak IPSC amplitudes versus stimulus intensity, the data points were grouped by eye based on IPSC amplitudes, and the average IPSC amplitude of each IPSC level was then calculated. The amplitude of unitary IPSCs was calculated as the difference between subsequent group averages (see e.g. Fig. 1A2). This gave an estimate of various unitary IPSC amplitudes in each recorded cell (Fig. 1C). For the conversion of IPSC amplitudes to conductance (Fig. 2), linear IPSC current - voltage relations between the holding potentials and the reversal potentials were assumed. For high $[Cl^-]_i$ (V_h = -70 mV) the average measured reversal potential (+4.5 mV; see Fig. 2C) was used for calculating conductance values. For low $[Cl^-]_i$, for 3 cells E_{rev} was determined in each cell, for one remaining cell the average measured E_{rev} was considered.

For the analysis of unitary IPSCs after weak optogenetic stimulation, the evoked IPSCs were analyzed only up to their first peaks (continuous traces in Fig. 3E1, E2, I), to avoid the possibility that a second AP in the *same* fiber could have biased the estimate of unitary IPSCs (by inducing short-term plasticity of the second IPSC).

Immunohistochemistry and confocal imaging

For immunohistochemistry, a *PV*^{Cre} x *ChR2* mouse (P 20; Fig. 3) and a *Math5Cre* x *ChR2* mouse (P 25; Fig. 5) were deeply anesthetized with intraperitoneal injection of pentobarbital (150 mg/kg body weight) and then transcardially perfused with 4% paraformaldehyde in phosphate-buffered saline solution. Immuno-staining of 40 µm thick transverse hindbrain sections on the level of the LSO was done as described before (Bouhours *et al.*, 2017). We used primary antibodies against VGAT (polyclonal guinea-pig, 1:500, cat. 131004; Synaptic Systems, Göttingen, Germany; RRID: AB_887873) or VGluT2 (polyclonal guinea-pig, 1:500, cat. 135404; Synaptic Systems; RRID:AB_887884) and GFP (polyclonal chicken, 1:1000; Abcam 13970, Cambridge, UK; RRID: AB_300798) to visualize the ChR2-eYFP protein. Primary antibodies were applied overnight at 4°C. The secondary fluorescently labelled antibodies (1h incubation at room temperature, dilution 1:200) were respectively, goat anti-guinea pig Alexa 647 (A21450; Thermofischer Scientific; RRID:AB_2535867) and goat anti-chicken Alexa 488 (A11039; Thermofischer Scientific; RRID: AB_2534096). Confocal images were acquired with an upright Zeiss LSM 700 microscope using the 488 and 633 nm laser lines and a Plan-Apochromat 40X/1.30 NA oil immersion objective (pixel size was 90 nm).

Model of E-I integration in an LSO neuron

To study the integration of excitatory and inhibitory synaptic inputs in LSO neurons in response to pure tone stimuli at both ears, we simulated a single integrate-and-fire neuron with correlated synaptic input (Gerstner *et al.*, 2014). The membrane voltage V in our model obeys the following differential equation:

$$C\frac{dV}{dt} = g_{\mathrm{leak}}(V_{\mathrm{rest}} - V) + g_{\mathrm{exc}}(V_{\mathrm{exc}} - V) + g_{\mathrm{inh}}(V_{\mathrm{inh}} - V)$$

with membrane capacitance C, leak conductance g_{leak} and resting potential V_{rest} (- 60 mV). Synaptic input is conductance-based with excitatory (and inhibitory) conductances g_{exc} (g_{inh}) and with V_{exc} = 0 mV and V_{inh} = - 80 mV denoting the reversal potentials of excitation and inhibition. Whenever the membrane potential reaches the threshold V_{thr} = -50 mV, a spike is emitted and in the next simulation time step the membrane potential is reset to V_{rest} where it remained during a refractory period of τ_{ref} = 1 ms. Afterwards, V evolved freely starting from V_{rest}.

In the absence of presynaptic spikes the synaptic conductances evolve independently according to the following set of differential equations:

$$\tau_{\mathrm{exc}} \frac{dg_{\mathrm{exc}}}{dt} = -g_{\mathrm{exc}} \text{ and } \tau_{\mathrm{inh}} \frac{dg_{\mathrm{inh}}}{dt} = -g_{\mathrm{inh}}$$

with synaptic time constants τ_{exc} = 1.5 ms and τ_{inh} = 3 ms respectively. At the arrival time of a spike in a given presynaptic excitatory fiber, g_{exc} makes a discontinuous transition $g_{exc} \rightarrow g_{exc} + \omega_{exc}$. Similarly a spike in a given inhibitory axon causes the transition $g_{inh} \rightarrow g_{inh} + \omega_{inh}$ to occur; here, ω_{exc} and ω_{inh} denote the unitary excitatory - and inhibitory conductances (0.7 and 9 nS for the simulations in case 1). The model cell had a capacitance of 15 pF and membrane time constant of 3 ms. Key parameters of the model are summarized in Figure 7B.

The model cell received synaptic input from a set of independently realized inhomogeneous Poisson processes. To mimic auditory stimuli as an input to our model, we used PSTHs with rectangular shapes and various peak firing rates for excitatory and inhibitory inputs (Fig. 7C, see Results for details). Each stimulation protocol was repeated 1000 times and the excitatory and inhibitory synaptic conductances and resulting membrane potentials were recorded for each trial (see e.g. Fig. 7D1; Fig. 7D2, top). These data were used to compute spike raster plots, the peri-stimulus time histogram (PSTH), and trial averaged firing rates, the latter two with 1ms binning, of the postsynaptic neuron (e.g. Fig. 7D2, middle and bottom). The simulations were performed using custom written C++ code base on the Auryn library (Zenke & Gerstner, 2014). Numerical integration was performed using the forward Euler method with a 0.1ms time step.

The rectangular PSTHs used as inputs to our model (see above) were deemed appropriate because in typical pure tone stimulation experiments during LSO in-vivo recordings, low intensity tones are used (Magnusson *et al.*, 2008; Karcz *et al.*, 2011). VCN bushy cells and MNTB neurons supposedly fire in a rather constant manner in response to low intensity sounds (Pfeiffer, 1966; Smith *et al.*, 1993; Kopp-Scheinpflug *et al.*, 2003). The spontaneous firing frequency of excitatory- and inhibitory axons was set to the conservative estimate of 10 Hz (Kopp-Scheinpflug *et al.*, 2003).

In the model, the number of excitatory (n = 40) and inhibitory inputs (n = 8) was larger than the number of inputs that we found in functional experiments (excitatory; n ~ 20; inhibitory; n ~ 5-6; see Figs. 5 and 1, respectively). The available evidence suggests that the number of inputs is typically larger than what can be measured in functional experiments (see also discussion in Gjoni et al., *accompanying manuscript*).

Statistics

Statistical tests were performed by using the software *Prism* (GraphPad, RRID: SCR_002798). Each data set to be tested statistically was first tested for normality by the D'Agostino and Pearson normality test. For all statistical tests (Figs 1G, 2D and 3L), we used the Mann-Whitney test because these data were not normally distributed.

We tested whether the logarithmized values of unitary IPSC amplitudes (Fig. 1E) might obey a normal distribution, by using the D'Agostino and Pearson test. In addition, we plotted the sorted logarithmic values against the normal order statistic median (the latter was calculated with a built-in function of IgorPro; Filliben, 1975), as a further graphical test for normality (Fig. 1F; Fig. 3H3).

Results

Large unitary IPSCs upon electrical stimulation of MNTB fibers

We wished to investigate the functional relevance of specific unitary IPSC and EPSC amplitudes for E-I integration in LSO neurons. We first measured IPSCs in LSO neurons after stimulating MNTB afferents electrically (Fig.1A), using young hearing mice for our study (P16 – P21). NBQX (or CNQX; both at10 µM) and D-APV (50 µM) were present in the bath solution to suppress EPSCs; for the experiments in Figs. 1 and 3, pipette solutions with high $[Cl^-]_i$ were used (see Methods). Fiber stimulation elicited fast-rising and decaying inward currents (decay time constant, 2.6 ± 0.9 ms when fitted with a single exponential; n = 9 cells). The currents were blocked by 2 µM strychnine (n = 3 cells; results not shown), suggesting that they were glycinergic IPSCs, in agreement with previous findings (Kotak *et al.*, 1998; Kim & Kandler, 2003, 2010; Walcher *et al.*, 2011; Hirtz *et al.*, 2012).

By varying the stimulation strength in small increments, we observed abrupt jumps between distinct IPSC amplitude levels in most recordings (Fig. 1A1, A2). We identified clear IPSC "steps" by visual inspection (Fig. 1A2; arrow indicates an example of a step; Kim & Kandler, 2003; Walcher *et al.*, 2011). In a few recordings, however, the IPSC amplitude increased more gradually over certain stimulation voltages, and steps could not be detected (Fig. 1B1, B2; IPSC amplitudes above ~ 3.5 nA in this case). We interpreted “steps” as the recruitment of a new fiber with increasing stimulation intensities, and used the step amplitudes to estimate the amplitudes of several unitary IPSCs in each recording (Fig. 1C).

The distribution of all unitary IPSC amplitudes (n = 42, from n = 9 recordings) showed a skew towards larger events and was significantly different from a normal distribution (Fig. 1D; p = 0.0388; D’Agostino and Pearson normality test). After logarithmic transformation of the data, the distribution was not significantly different from a normal distribution (Fig. 1E; p = 0.117; D’Agostino and Pearson Normality test), suggesting that the unitary IPSCs might obey a log-Normal distribution. The logarithmic transformation also revealed that there were some small events not well fitted by the Gaussian (Fig. 1E). As a further test, we plotted the sorted and logarithmically transformed unitary IPSCs amplitudes against the normal order statistic median, which graphically suggested a log-normal distribution (Fig. 1F). The average unitary IPSC was 2.06 ± 1.84 nA (mean ± S.D., n = 42 unitary IPSCs in n = 9 recordings), with a median of 1.73 nA. These values of unitary IPSCs are larger than in most previous studies (Kim & Kandler, 2003, 2010; Noh *et al.*, 2010; Hirtz *et al.*, 2012; but see Walcher *et al.*, 2011; see Discussion for an exact comparison with the previous studies).

When we plotted the amplitude of unitary IPSCs in the order of their occurrence with increasing stimulation intensity, we found that unitary IPSC amplitudes tended to increase with increasing stimulus intensity (Fig. 1G; note the logarithmic scale). Thus, the unitary IPSCs at threshold (0.37 ± 0.39 nA) had a significantly smaller amplitude than the fifth-appearing unitary IPSCs (3.7 ± 1.6 nA; Fig. 1G; average data points; $p < 0.001$, Mann-Whitney test; see Discussion). The IPSC amplitude recorded at the highest stimulation intensities was on average 11.3 ± 5.6 nA across recordings (Figs 1A2, B2; n = 9), ~ 2 - 3 fold larger than the previously reported maximal IPSC values (Kim & Kandler, 2003, 2010; Noh *et al.*, 2010; Hirtz *et al.*, 2012; Clause *et al.*, 2014).

Since the IPSC amplitudes were large, voltage-clamp errors are a possible concern. In our recordings, we attempted to impose successful voltage-clamp by minimizing series resistances (R_s); by electronically compensating for part of the R_s during the recordings (50 - 90%), and by correcting the remaining R_s error off-line (Meyer *et al.*, 2001; see Methods). An example for offline-R_s compensation is shown in Fig. 1A3 (red trace). In the case of the 40 V stimulation, the increase of the IPSC amplitude caused by the offline R_s-compensation was more than 50 % and therefore, the corresponding data points were not admitted for the final data set (red data points in Fig. 1A2; see also Methods). Thus, we estimate that voltage-clamp errors caused by the large current flow during these IPSCs can be substantial, and that online- and offline compensation of R_s errors must be employed to estimate correct IPSC amplitudes, especially at high stimulation intensities when IPSCs are large. Taken together, the experiments in Fig. 1 suggest that unitary IPSCs at the MNTB - LSO synapse are larger than previously estimated, and that unitary IPSC amplitudes in a given LSO neuron are distributed over a wide range (~ 10 -fold).

We also measured the conductance of unitary IPSCs under conditions of low, near-physiological $[Cl^-]_i$ (Ehrlich *et al.*, 1999). With 6 mM $[Cl^-]_i$, the reversal potential was strongly shifted towards negative values (-76.2 ± 6.3 mV), as expected for a Cl^- conductance (Fig. 2A-C). Under these conditions, we measured IPSCs at a holding potential of - 50 mV, and upon increasing the stimulation intensity gradually, steps could again be distinguished in many recordings (Fig. 2A1, A2). We then computed the conductance of unitary ISPC from the step amplitudes observed at - 50mV and taking into account the reversal potential of the IPSCs (see Methods). This yielded an average unitary IPSC conductance of 9.1 ± 6.9 nS across cells (n = 11 unitary IPSCs in n = 4 recordings; Fig. 2D, *left*). This value was roughly 3 -fold smaller than the unitary IPSC conductance, which we computed for the data from Fig. 1 obtained under high $[Cl^-]_i$ (31.8 ± 27.6 nS; n = 42 unitary IPSCs; Fig. 2D, *right*). Thus, low $[Cl^-]_i$ leads to a shift of the reversal potential, and it furthermore reduces the conductance of unitary IPSCs by a factor of roughly 3. Indeed, this factor is consistent with single-channel measurements of glycine- and $GABA_A$ - receptor channels under conditions of low $[Cl^-]_i$ (Bormann *et al.*, 1987). For the simulations in Fig. 7, we used the physiologically more relevant value of 9 nS for the conductance of an average unitary IPSC (see below).

Optogenetic stimulation to estimate unitary IPSC amplitudes

We wished to confirm the estimate of large unitary IPSC amplitudes using an independent stimulation method, and therefore turned to optogenetic stimulation of afferent fibers (Boyden *et al.*, 2005; Petreanu *et al.*, 2007). We crossed a PV^{Cre} mouse line (Hippenmeyer *et al.*, 2005) with a Channelrhodopsin - eYFP reporter mouse line (called *ChR2* below; Madisen *et al.*, 2012) to drive ChR2 expression in axons arising from the MNTB, based on the observation that MNTB principal neurons express PV (Lohmann & Friauf, 1996; Felmy & Schneggenburger, 2004). Because excitatory nerve terminals arising from the VCN will also be stimulated in the PV^{Cre} x *ChR2* mice (see below; Fig. 4), we measured optogenetically evoked IPSCs in the presence of CNQX (10 µM) and D-APV (50 µM). Immunohistochemistry with antibodies against GFP (to enhance the eYFP-signal of the ChR2-eYFP construct) and VGAT revealed the presence of ChR2 on the membranes of inhibitory nerve terminals surrounding LSO neurons (Fig. 3B).

We recorded from LSO neurons under conditions of high $[Cl^-]_i$ and at a holding potential of –70 mV. Low-intensity blue light pulses (1 ms) in the tissue surrounding the recorded LSO neuron triggered desynchronized IPSCs with multi-peak appearance (Fig. 3C1). Upon increasing the light intensity, the IPSC amplitudes became larger, and the compound IPSCs became gradually more phasic until their rising phase reached sub-millisecond kinetics (Fig. 3C2). In addition, the latency of the IPSCs became substantially shorter (Fig. 3D; see Discussion). When the rising phases of the IPSCs were nearly synchronous, the measured compound IPSCs caused in all recordings a saturation of the patch-clamp amplifier at 20 nA (n = 5 recordings). Considering the R_s errors, a lower-limit estimate of these ISPCs evoked by maximal optogenetic stimulation of ~ 30 nA results (see also Methods). For the recording in Fig. 3C2, we reduced the holding potential to -20 mV to allow the recording of a non-saturating IPSC in response to strong optogenetic stimulation, but we emphasize that this IPSC was too large to be voltage-clamped. These large IPSCs were not caused by direct optogenetic depolarization of the nerve terminal since they were completely suppressed by adding 1 µM tetrodotoxin (results not shown, and see Bouhours *et al.*, 2017). Taken together, maximal optogenetic stimulation suggests that the total strength of inhibition mediated by the sum of potentially all PV - positive inhibitory fibers that innervate a given LSO neuron is substantially larger than previously estimated (see Discussion).

We next developed protocols of minimal optogenetic stimulation to assess the unitary IPSC amplitudes (Fig. 3E). In a first protocol, we used weak light pulses (1.0 - 2.5 % of maximal LED light) with a short duration (1 ms), with the aim to evoke IPSCs at the stimulation threshold, and occasional failures (see Fig. 3E1 for two light intensities in one recording). In some experiments, we additionally or alternatively used prolonged light pulses (5 ms) at even lower light intensities (< 0.5 %; Fig. 3E2). Both types of minimal optogenetic stimuli desynchronized the activation of presynaptic fibers, which enabled us to temporally resolve fast-rising IPSCs. These most likely represent the firing of individual presynaptic fibers, and therefore, unitary IPSCs. We restricted the analysis to the first peaks of fast-rising IPSCs (Fig. 3E; continuous trace). The resulting amplitude histograms showed various peaks, which were fitted with multi-peak Gaussian functions; the center of each Gaussian component was taken as an estimate of a unitary IPSC (Fig. 3F). In the example recording of Fig. 3E, the unitary IPSCs had amplitudes of 0.53, 2, 5, 10.1 and 18.2 nA (Fig. 3F, and Fig. 3G, cell # 1).

Across cells, minimal optogenetic stimulation revealed unitary IPSC amplitudes with a large variation in each recording, with a characteristic spread over an about 10 -fold range (Fig. 3G, H1). The distribution of logarithmized unitary IPSC amplitudes collected from all recordings was again not significantly different from a normal distribution (Fig. 3H2; p = 0.1842; D’Agostino and Pearson test), and was graphically determined to be log-normally distributed (Fig. 3H3). The mean and S.D. of the unitary IPSC amplitudes was 5.2 ± 4.5 nA (n = 45 unitary IPSCs from n = 11 recordings; median, 4.1 nA); this value was larger than the unitary IPSCs estimated by the fiber stimulation method (Fig. 1; mean of ~ 2 nA).

To reconcile the larger estimates of unitary IPSCs after optogenetic stimulation, we next wished to more selectively stimulate afferent fibers arising in the MNTB. For this purpose, we moved the site of optogenetic stimulation to the ipsilateral MNTB in some recordings, and again applied minimal optic stimuli (Fig. 3I). These experiments yielded a smaller estimate of unitary IPSC amplitudes (2.0 ± 1.9 nA; n = 29 unitary IPSCs from = 7 recordings; Fig. 3I-K).

There might be two reasons for the larger unitary IPSC amplitudes after local optogenetic stimulation in the LSO. First, local stimulation of axons might evoke release with a higher release probability, maybe caused by broader axonal APs (Zhang & Oertner, 2007). Second, PV-positive inhibitory axons of a non-MNTB origin might innervate LSO (see e.g. Jalabi *et al.*, 2013), and it is conceivable that these fibers have larger unitary IPSCs than fibers originating in the MNTB. Nevertheless, we note that minimal optogenetic stimulation in the MNTB leads to a similar estimate of unitary IPSC amplitudes as with fiber stimulation (~ 2 nA in each case).

Optogenetic estimate of unitary EPSC amplitude

To address how unitary IPSCs with overall large, but variable amplitude inhibit the firing of LSO neurons, we next sought to obtain information about the excitatory input that drives AP firing in LSO neurons. Previous work has shown that electrical fiber stimulation laterally to the LSO, presumably activating fibers of the VCN - LSO connection, leads to EPSCs of moderate total amplitude, with an overall rather graded nature (Case & Gillespie, 2011; Xiao *et al.*, 2013; Felix & Magnusson, 2016; but see Discussion). Here, we used optogenetic stimulation of the VCN to LSO pathway, to enable the selective stimulation of molecularly identified afferent fibers.

In a first series of experiments (Fig. 4), we used the PV^{Cre} x *ChR2* mice, because bushy cells in the VCN express PV (Lohmann & Friauf, 1996; Xiao *et al.*, 2010). Since optogenetic stimulation under the PV promoter also leads to activation of glycinergic fibers from the MNTB (Fig. 3), the experiments were done in the presence of 2 µM Strychnine and 10 µM Bicuculline to block IPSCs. In striking difference to the optogenetically stimulated IPSCs, we observed small EPSCs at the threshold for successful stimulation (26.2 ± 11.0 pA; n = 9 recordings; Fig. 4A1, B, C). In some recordings, we noted an early-rising but more slowly decaying photocurrent probably due to the expression of ChR2 in some LSO neurons of the *PV*^{Cre} x *ChR2* mice (Fig. 4A1, pink trace which did not contain an EPSC). In a few recordings, we increased the light intensity to measure more complete input - output curves, but we did not observe clear step-like increases of EPSCs (Fig. 4A2; see also Fig. 5). Thus, optogenetic stimulation experiments under the PV promoter suggest a small unitary EPSC amplitude measured at the threshold for stimulation, and a small total synaptic weight of EPSCs mediated by PV-positive excitatory axons.

Integration of many small unitary EPSCs in LSO neurons

We next took advantage of the *Math5* promoter (Saul *et al.*, 2008) to optogenetically stimulate the excitatory inputs from bushy cells more selectively. We crossed *Math5*^{Cre} with *ChR2* mice, and investigated the presence of ChR2 - positive axons by immunohistochemistry in the LSO (Fig. 5B). This revealed ChR2-eYFP (Math5) - positive axons in the LSO; many but not all of these axons contained vGluT2 - positive nerve terminals (Fig. 5B, *right*). This is consistent with the finding that most bushy cells co-express the mRNA for both vGluT1- and -2 isoforms, but that some are VGluT2 - negative (Xiao *et al.*, 2010).

We then made recordings of LSO neurons and stimulated Math5-positive nerve terminals optogenetically, with the aim to estimate unitary EPSC amplitudes, and to investigate the number of unitary EPSCs necessary to trigger an AP in an LSO neuron. Brief blue light pulses (1 ms) evoked small EPSCs at the threshold for successful stimulation (Fig. 5C2, left; 44.5 ±

9.7 pA on average in n = 6 recordings; Fig. 5F, *left*). The EPSC amplitude rose gradually with increasing light intensity (Fig. 5C2, D2). These data suggest that similarly as with optogenetic stimulation under the PV-promoter (Fig. 4), unitary EPSCs were small.

We performed the same measurements under current-clamp, to investigate the number of unitary EPSCs needed to trigger an AP in an LSO neuron. This showed that EPSP amplitudes increased gradually until at ~ 10 - 15 mV, an AP was triggered (Fig. 5C1, D1). Comparison with the EPSC input-output curve under voltage-clamp shows that in this recording, an EPSC of ~ 220 pA amplitude was needed to reliably trigger an AP in the three repeated trials (Fig. 5D1, D2). Across all recordings this value was 258 ± 82 pA (Fig. 5F, *right*; n = 6 recordings). Considering the estimated unitary EPSC amplitude (~ 44 pA; see above), it is seen that ~ 5 - 7 unitary excitatory inputs need to be active synchronously to trigger an AP in an LSO neuron. At high light intensities, optical stimuli led to EPSCs with near - saturating amplitudes of 0.93 ± 0.59 nA (Fig. 5E, 5G, *right*; n = 6). Considering the unitary EPSC amplitude measured in each recording, we estimate that the EPSCs at maximal amplitude were carried by 20 ± 10 unitary excitatory inputs (Fig. 5G, left).

Taken together, the optogenetic stimulation results in Figs 4 and 5 show that LSO neurons receive a graded excitatory input from VCN bushy cells without obvious steps. The unitary EPSC amplitude based on minimal stimulation is ~ 30 - 45 pA, corresponding to a conductance of ~ 0.7 nS. This value is significantly smaller than the average unitary inhibitory conductance of ~ 9 nS (Figs. 1, 2). Also, maximal optogenetic stimulation of excitatory fibers under both promoters led to compound EPSCs of ~ 1 nA, in strong contrast to optogenetic stimulation of inhibition, which showed maximal IPSCs of 20 nA or larger (see above).

The inhibitory conductance required to suppress AP firing

Previous current-clamp recordings have shown that electrical stimulation of inhibitory synapses to LSO neurons inhibits AP firing during a short effective time window (Sanes, 1990; Wu & Kelly, 1992). Here, we determined how converging excitatory, and inhibitory inputs influence the firing of an LSO neuron. We first assessed the strength of inhibition necessary to suppress AP firing driven by supra-threshold excitatory inputs from bushy cells. For this purpose, we made recordings under near - physiological $[Cl^-]_i$ conditions (6 mM), and stimulated the excitatory bushy cell inputs optogenetically using the *Math5*^{Cre} x *ChR2* mice, while the MNTB – LSO inhibitory synapse was activated via electrical fiber stimulation.

We first measured the input-output curves for IPSCs and for EPSCs in voltage-clamp, to find suitable stimulation strengths for the E – I integration experiment. In the example recording of Fig. 6A-C, an optical stimulation with 10 % of the maximal LED light evoked a supra-threshold EPSP that reliably triggered an AP as measured under current clamp (Fig. 6A1, *top*). In this recording, the electrical stimulation intensities for the MNTB fibers were 5 V and 18 V, which triggered a small IPSC (0.31 nA, or 12.3 nS), and a larger IPSC (0.87 nA / 33.5 nS) (Fig. 6A2). We then varied the timing of excitation relative to inhibition to explore at which relative timing inhibition is most successful. When the onset of the IPSP was nearly coincident with the start of the EPSP, the IPSP effectively suppressed AP generation (Fig. 6B; Δt values of -1.4 ms and -0.4 ms). However, when the EPSP occurred only a few milliseconds *after* the start of the IPSP, the former could again trigger an AP (Fig. 6B bottom; Δt values +1.6, + 2.1 ms).

We plotted the AP success rate, estimated from n = 5 repetitions, as a function of the relative timing of EPSPs and IPSPs (Fig. 6C). For the example recording of Fig. 6A-B, in which the effect of a stronger intensity for stimulating inhibitory fibers was tested (33.5 nS), a time of 3.2 ms became apparent during which the IPSP completely suppressed AP firing (Fig. 6B; star symbols; Fig. 6C, red data points). In the same recording, weak stimulation that evoked a small

IPSC of 12.3 nS could only partially lower the probability for an AP (Fig. 6C; pink data points). In all recorded cells, the width of the effective inhibition window was a function of the inhibitory conductance (Fig. 6D). Furthermore, this plot shows that an inhibitory conductance of ~ 10 nS was necessary to start causing a suppression of AP firing.

At the end of each experiment, we also varied the excitation strength, in combination with two of the investigated inhibitory conductances. Increasing the EPSC conductance led in all cases to a shortening of the effective inhibition window (Fig. 6D, data points connected by dashed lines). In a few cases the increased excitation was able to overcome the inhibition completely as in the example of the yellow data points in Fig. 6D (inhibition window dropped to 0).

In Fig. 6E, the width of the effective inhibition window was plotted as a function of the *ratio* of inhibitory - over excitatory conductance. This re-normalized the appearance of the data points obtained under stronger excitation by shifting them leftwards on the abscissa. This plot shows more clearly that in order to achieve an effective inhibition window of 1 - 3 ms, the inhibitory conductance had to be ~ two times higher than the excitatory one (Fig. 6E, grey shaded area).

We also compared the length of the effective inhibition window to the half-width of the IPSCs and of the IPSPs (Fig. 6F). In general, the effective inhibition window fell in-between the IPSCs and IPSP half-width, except for very small inhibitory conductances which were unable to cause a suppression of AP triggering at all. In a few recordings, like the one shown in Fig. 6A-C, the inhibition window (3.2 ms) was nearly as short as the half-width of the IPSCs (2.2 ms; both values for the larger IPSC of 33.5 nS in Fig. 6A-C). This was reminiscent of classical shunting inhibition during which inhibition is only effective when the inhibitory conductance is active (Fatt & Katz, 1953). However, in other recordings the length of the effective inhibition window was closer to the half-width of the IPSP, but it never clearly exceeded the latter (Fig.

6F). Thus, we conclude that even substantial inhibitory conductances of several tens of nS, can only briefly, for 1 - 3 ms, suppress AP firing caused by suprathreshold bushy cell inputs in LSO neurons.

A connectivity-based model of E - I integration in the LSO

We found that LSO neurons receive overall large inhibitory inputs with a large fiber-to-fiber variability in amplitude, whereas unitary excitatory inputs are weak and graded in nature. We wished to explore the role of this afferent input connectivity in generating the tuning curve of LSO neurons *in-vivo*. For this purpose, we developed a connectivity-based model of E - I integration. We used a simplified integrate-and-fire point-neuron model (Gerstner *et al.*, 2014) to concentrate on modelling the influence of the unitary synaptic strength and fiber convergence of both the excitatory and inhibitory inputs (Fig. 7).

We wished to model *in-vivo* recording experiments of LSO neurons (Magnusson *et al.*, 2008; Karcz *et al.*, 2011). In these, sound stimulation of the ipsilateral ear is typically applied with constant amplitudes slightly above threshold, while the sound intensity at the contralateral ear is varied for each trial. Most parameters were taken, or slightly adapted from our experimental observations (Fig. 7B; see also Methods). Fig. 7C shows the modeled "input" firing rates of excitatory and inhibitory presynaptic axons in response to three simulated sound presentations. We simulated constant sound intensity at the ipsilateral ear (thus, constant firing rates of the excitatory fibers; Fig. 7C1), whereas the firing of the inhibitory afferents was modulated from 10 Hz, the assumed spontaneous firing rate in the absence of sound, to 30, 60, 90 and 120 Hz.

Fig. 7D1 shows the modelled postsynaptic conductances in response to the firing of the excitatory and inhibitory afferent fibers. For the standard model ("case 1"), there were n = 8 inhibitory inputs whose weights were evenly spaced on a log scale with a mean g_{inh} of 9 nS

(Fig. 7C2), and n = 40 excitatory inputs with 0.7 nS each. With a weak activity of the inhibitory afferents (30 Hz), the excitatory inputs caused vigorous firing of the LSO neuron (Fig. 7D2, *left*). With increasing firing rates of the inhibitory afferents (see Fig. 7C), the firing frequency was suppressed, except for a brief response at the onset of the sound (Fig. 7D2, *middle* and *right*), which is also observed *in-vivo* (Magnusson *et al.*, 2008). In the absence of sound stimulation, large negative fluctuations of V_m were apparent which were caused by spontaneous IPSPs (Fig. 7D2, V_m trace at top); these caused a tail towards more negative values in the histogram of the V_m values (Fig. 7D2, inset).

To explore the computational significance of few, but strong inhibitory inputs, we next simulated the opposite case, i.e. a case in which the total inhibitory conductance (total g_{inh} = 72 nS) was distributed over many small inhibitory inputs ("case 2", N_{inh} = 40, unitary g_{inh} = 1.8 nS). With these parameters, individual IPSPs were less discernible, and the distribution of V_m values at rest showed only a single peak (Fig. 7E2, inset). Under sound stimulation with an ipsilaterally louder sound (excitatory fibers: 60 Hz, inhibitory: 30 Hz), the firing rate response was much lower (~ 25 Hz) as compared to case 1 (compare Figs. 7E2 and D2; note different scales). In the regime of equally intense sounds and for contralaterally louder sounds, the firing responses were strongly inhibited, except for a brief AP response at the onset (Fig. 7E2, *middle*, *right*). This led to a strongly suppressed evoked firing rate in the resulting tuning curve, except for the weakest contralateral sounds (Fig. 7G, compare case 2 with case 1; see also Fig. 7H in which the convergence of inhibitory inputs was varied over a larger range). These simulations indicate that many, but proportionally weaker unitary inhibitory inputs put a temporally more uniform "blanket" of inhibition on LSO neurons, which causes a shift of the tuning curve towards ipsilaterally louder sounds.

We modelled a third case, to explore the computational significance of the innervation of LSO neurons by many, but small excitatory inputs. Assuming the standard case for inhibition (N = 8 inhibitory inputs with amplitudes evenly spaced on a log scale), we then decreased the number of excitatory inputs to n = 8, and increased the unitary excitatory strength to g_{exc} = 3.5 nS to keep the total excitatory conductance constant. The resulting tuning curve was not strongly changed as compared to the standard case (case 1; Fig. 7G). However, the spontaneous firing rate in the absence of sound was strongly increased to 23 ± 7.9 Hz, whereas in the standard case, it was 2.8 ± 2.6 Hz (Fig. 7F). The spontaneous firing rates of ~ 3 Hz modelled in case1 is close to the observed value for LSO neurons (Tsuchitani & Boudreau, 1966; Karcz *et al.*, 2011). Indeed, systematically varying the number of excitatory inputs revealed a strong effect of this parameter on the spontaneous firing rate of the LSO neuron (Fig. 7I, left). This can be understood by considering that spontaneous EPSPs with a larger amplitude will reach the AP threshold more easily; the smaller *frequency* of excitatory events upon decreasing the convergence (fewer excitatory fibers) could apparently not compensate for this effect, as expected because of the fast membrane time constant of these non-integrating neurons.

Finally, we modelled a fourth case, in which we assumed N = 8 inhibitory inputs as in case 1, but in which we now assumed that inhibitory inputs had a fixed amplitude of 9 nS (Fig. 7J; case 4). This simulation produced slightly smaller AP firing rates with ipsilaterally louder sounds as compared to case 1 with log-normally distributed unitary IPSC amplitudes (see Discussion); the spontaneous AP firing rate was essentially unchanged as compared to case 1 (Fig. 7F). Taken together, a connectivity-based model shows that the specific strength, and convergence of both the excitatory and inhibitory inputs determines E - I integration, and spontaneous firing rates in LSO neurons.

Discussion

LSO neurons integrate ipsilateral excitation with contralateral inhibition to generate AP firing which codes for interaural sound intensity differences (Boudreau & Tsuchitani, 1968; Caird & Klinke, 1983; Sanes, 1990; Kim & Kandler, 2003; Magnusson *et al.*, 2008; Karcz *et al.*, 2011). Nevertheless, how exactly excitation and inhibition are integrated in the LSO, and the role of the specific unitary synaptic strengths in this process, has received little attention. We found that a given LSO neuron typically receives unitary IPSCs with different amplitudes that roughly obey a log-normal distribution. The amplitudes of the IPSCs were large, with a median of ~ 1.7 nA under high $[Cl^-]_i$, and a mean conductance of ~ 9 nS under near - physiological conditions of low $[Cl^-]_i$. On the other hand, optogenetic stimulation of Math5-positive bushy cell axons produced graded EPSCs without obvious steps, and the unitary EPSC estimated by minimal stimulation was small (~ 0.7 nS). Thus, in the LSO, a multitude of weak unitary excitatory inputs is integrated with strong unitary inhibition distributed over fewer inputs. We found by modelling that this convergence of unitary inhibitory - and excitatory input strengths is a key determinant of the tuning curve that results from E - I integration in LSO neurons.

Strong but variable unitary inhibition onto LSO neurons

Previous fiber-stimulation experiments in LSO after ~ P9 have shown discrete steps in the IPSC amplitudes when the stimulation strength was gradually increased (Kim & Kandler, 2003; Walcher *et al.*, 2011; Hirtz *et al.*, 2012). We observed "step" amplitudes that varied over a roughly 10-fold range in a given recording, from a few 100 of pA to several nanoamperes. Furthermore, we found that small unitary IPSCs of a few hundred pA preferentially occurred at low stimulation intensities whereas higher unitary IPSCs were visible with stronger stimulation intensity (Fig. 1G), by a yet unknown mechanism. The value we obtained at stimulation threshold agrees with previous studies that often focused on the first-appearing step (~ 250 pA, Hirtz *et al.*, 2012; ~ 500 pA, Kim & Kandler, 2010; Noh *et al.*, 2010; Clause *et al.*, 2014; ~ 700 pA, Kim & Kandler, 2003). However, the amplitudes of all subsequent steps (second to fifth unitary IPSCs; 2.83 ± 2 nA in our study; Fig. 1G) were significantly larger than the previous estimates of unitary IPSCs based on minimal stimulation. Thus, we conclude that both the median amplitude of unitary IPSCs, as well as the variability of unitary IPSC amplitudes is larger than previously thought. It is possible that voltage-clamp limitations, which should be more severe for the late-occurring larger unitary IPSCs, as well as the focus on the first-appearing unitary IPSCs are factors that contribute to the smaller estimates of unitary IPSC amplitudes in the previous studies. One study found a value of 18 nS for the unitary IPSC conductance under conditions of physiological $[Cl^-]_i$, which is comparable or even larger than our estimate (Walcher *et al.*, 2011). However, another recent study found small estimates even of *total* inhibitory conductance (~ 5 nS; Pilati *et al.*, 2016).

We used optogenetic stimulation of presynaptic fibers (Boyden *et al.*, 2005; Petreanu *et al.*, 2007) to measure unitary IPSCs with an independent approach. Variation of the light intensity at the threshold for successful stimulation evoked large unitary IPSCs that appeared as fast-rising, but temporally de-synchronized events. Higher stimulation intensities significantly shortened the delay of evoked IPSCs (Fig. 3D); similar observations were made for the optogenetically evoked EPSCs (Fig. 4A1; Fig. 5C2). The longer delay with lower light stimulation and the temporal variance in the occurrence of unitary IPSCs is probably caused by small presynaptic ChR2 currents, that lead to slow and variable presynaptic AP threshold crossings. This phenomenon has allowed us to temporally isolate discrete, fast-rising unitary IPSC events, which in LSO neurons can reach several nA of amplitude (Fig. 3). When studying excitatory transmission with the same method, we exclusively observed small events in the tens of picoampere range (Figs 4, 5). This revealed a striking, about 30-fold difference in the *unitary* synaptic conductances between inhibition and excitation converging onto LSO neurons, at least when excitation and inhibition are both measured under conditions of high driving forces (~ 70 mV). The minimal optogenetic stimulation method used here might also be useful to measure the strength of unitary synaptic events in other circuits, similar to what has been done recently at other connections (Lu & Trussell, 2016; Litvina & Chen, 2017).

To translate to more physiological conditions, we measured unitary IPSCs under conditions of low $[Cl^-]_i$, which is normally prevalent especially in auditory neurons (Ehrlich *et al.*, 1999; Kopp-Scheinpflug *et al.*, 2011). Under these conditions, the unitary IPSC *conductance* was about 3-times smaller than under high $[Cl^-]_i$ (Fig. 2). This reduced unitary inhibitory conductance is explained by the outward rectification and a smaller conductance of single glycine- (and $GABA_A$) receptors under low intracellular permeant ion concentrations close to the reversal potential (Bormann *et al.*, 1987). This illustrates that inhibitory receptors are constrained to function in a submaximal range, because inhibition normally has to function at membrane potentials not far from the reversal potential of these anion channels. Several mechanisms might compensate for this biophysical limitation, including a large single-channel conductance of glycine receptors in general (Bormann *et al.*, 1993), a high density of postsynaptic glycine receptors (Friauf *et al.*, 1997; Hruskova *et al.*, 2012) thus creating large quantal amplitudes (Kim & Kandler, 2010), and the elaboration of multiple active zones by inhibitory axons enabling the generation of multiquantal IPSCs (Gjoni *et al.*, accompanying manuscript).

What might be the basis for the variable, but overall large strength of unitary inhibitory inputs onto a given LSO neuron? We have used SBEM to reconstruct the inhibitory axons that make contact with the soma and proximal dendritic segments of an LSO neuron (Gjoni *et al.*, accompanying manuscript). We found that inhibitory axons establish large varicosities (average diameter, 3.7 µm) most of which contain several active zones. The number of repeated varicosities per axon, and therefore also the total number of active zones strongly varied between individual axons. This, together with a constant quantal size between "small" and "large" unitary IPSCs estimated by the Sr^{2+} method (Gjoni *et al.*, accompanying manuscript), strongly suggests that "small" and "large" unitary IPSCs are primarily distinguished by the number of active zones which they establish with an LSO neuron. Furthermore, when studying younger LSO neurons with fiber stimulation, we found that the characteristic ~ ten-fold variation between inputs is already found at ~ P7, despite an overall weaker total inhibition strength in pre-hearing mice (smaller maximal IPSCs; data not shown). It will be interesting to further study the developmental plasticity mechanisms - which could depend on pre-hearing activity in the auditory system (Sanes & Takacs, 1993; Clause *et al.*, 2014) - responsible for the coordinated growth of inhibitory axons onto a given LSO neuron.

Many weak excitatory bushy cell inputs converge onto an LSO neuron

Optogenetic stimulation under the bushy cell-specific Math5 promoter (Saul *et al.*, 2008; Kronander *et al.*, 2017) revealed small EPSCs of ~ 50 pA amplitudes at the threshold for successful stimulation (Fig. 5); similar observations were made with optogenetic stimulation of excitatory inputs under the PV promoter (Fig. 4). Furthermore, the input-output curves appeared graded, suggesting that the unitary EPSC amplitudes were too small to be detected as clear steps. This data seems different from two previous studies which used electrical fiber stimulation in developing mice (Felix & Magnusson, 2016) and rats (Case *et al.*, 2011). These studies reported steps of ~ 200 pA amplitudes especially in the older age groups (around hearing onset). We do not think that the absence of obvious steps in our data was a developmental issue, because our recordings were done at in young hearing mice (P16 - P21). Furthermore, in three additional recordings in *Math5Cre* x *ChR2* mice in which we measured optogenetic input-output curves in much older mice (P40 and P68), we did not observe clear steps either (data not shown). Thus, species differences, or differences between optogenetic stimulation used here, and the fiber stimulation used in the previous studies, might account for the different results. Taken together, we conclude that the bushy cell inputs onto LSO neurons have an overall graded nature in post-hearing mice.

The effective window of inhibition in LSO neurons is brief

In double stimulation experiments with optogenetic - and electrical stimulation (Fig. 6), we found that inhibition of AP firing was limited to a brief time window of ~ 1 - 3 ms, in agreement with previous current-clamp studies *in-vitro* (Sanes, 1990; Wu & Kelly, 1992). It is likely that *in-vivo* and at physiological temperatures, the inhibitory window is shorter and falls in the sub-millisecond range, as is suggested by recent *in-vivo* recordings in gerbils (Beiderbeck *et al.*, 2018). We showed with voltage-clamp measurements that the inhibitory conductance needed to be ~ 2-fold larger than the excitatory one to guarantee suppression of AP firing driven by bushy cell inputs (Fig. 6E). These experiments roughly indicate that a spike triggered by an excitatory synaptic conductance of ~ 7 nS (Fig. 6D), or by about 10 excitatory fibers, might not be efficiently inhibited by a single "small" unitary IPSCs (< 9 nS). Conversely, a unitary IPSC of the "large" class (> 9 nS), or two synchronously occurring unitary IPSCs, will most likely suppress firing for a few milliseconds.

LSO neurons in post-hearing mice have a fast membrane time constants of a few milliseconds (Walcher *et al.*, 2011). Thus, the duration of the IPSP caused by a single or a few synchronously occurring unitary IPSCs should be short. In agreement with this prediction, we found short IPSP half-widths generally in the range of 2 - 6 ms. The effective inhibition window was still shorter, in the range of 1 - 3 ms (or 5 ms in one case; Fig. 6F). The brief window of inhibition might be caused by several factors, such as shunting inhibition, i.e. effective inhibition is limited to the time of active inhibitory conductance (Fatt & Katz, 1953). Additionally, active mechanisms in the postsynaptic neuron like I_h currents which are found in LSO neurons (Koch *et al.*, 2004), or accelerated recovery of Na^+ channel inactivation after strong hyperpolarization, could act to limit the effective inhibition window in LSO neurons (Leao *et al.*, 2011).

Computational role of large unitary inhibition versus small unitary excitation in E - I integration

We developed a connectivity-based model to investigate how the observed convergence of inhibitory- and excitatory inputs shapes the output activity of LSO neurons. Although E - I integration in the LSO has inspired many modelling studies (for example, Reed & Blum, 1990; Karcz *et al.*, 2011; see Ashida *et al.*, 2017 for a systematic comparison of many previous models), synaptic input strength- and convergence parameters were not investigated in past modeling studies (see also discussion in Ashida *et al.*, 2017). We chose a simple integrate-and-fire model which allowed us to focus on the influence of unitary afferent synaptic strength, and the degree of convergence in both the excitatory and inhibitory pathways, on E-I integration in LSO neurons. The simulations showed that varying the convergence of inhibitory inputs strongly determines the steepness of the LSO tuning curve. Thus, many but weak inhibitory afferents, a parameter set opposite to the experimentally observed situation, led to a quenching of LSO neuron firing over a large range of ipsi- and contralateral sound intensities (Fig. 7G, H). This can be understood intuitively by considering that a large number of inhibitory fibers will cause many (albeit proportionally smaller) inhibitory events per unit time, creating a time-uniform inhibitory 'blanket'. Conversely, fewer inhibitory fibers with larger amplitude cause more stochastic variation in the membrane potential and deeper hyperpolarizations (Fig. 7D, E). These, upon repolarization, can more readily trigger an AP consistent with our experimental results (Fig. 6), and with recent *in-vivo* findings (Beiderbeck *et al.*, 2018). In our simulations with a simple integrate-and-fire model, the difference between large constant unitary ISPCs, and the more realistically large unitary IPSCs with *variable* amplitudes was not large (Fig. 7J). It is possible that the effect of unitary IPSC variability would be more visible when active conductances, and a more realistic subcellular distribution of inhibitory - and excitatory inputs would be present in the model.

Bushy cells in the VCN show high spontaneous firing rates in the absence of sound (Smith *et al.*, 1993, 1998; Kopp-Scheinpflug *et al.*, 2003), because they are driven by auditory nerve fibers, some of which show high spontaneous rates (Liberman, 1978). One aspect of connecting a bushy cell to a downstream neuron via many, but small excitatory connections is that the elevated spontaneous activity is filtered out as we show here by modeling (Fig. 7I). Indeed, the observed spontaneous activity of LSO neurons of a few Hz *in-vivo* (Tsuchitani & Boudreau, 1966; Karcz *et al.*, 2011) is substantially lower than the one of bushy cells, which is more on the order of 10 - 50 Hz (Smith *et al.*, 1993; Kopp-Scheinpflug *et al.*, 2003). Therefore, the convergence of many, but small excitatory inputs contributes to a steep tuning curve (Fig. 7I, right) and acts to filter out the elevated spontaneous activity of bushy cells.

The convergence patterns of excitation and inhibition that we found here for mouse LSO neurons might not necessarily be shared by other binaural neurons like the medial superior olive (MSO). Indeed, a recent *in-vitro* study in the MSO of gerbils also found strong unitary inhibition, but different to the present study, few but large excitatory inputs which matched the inhibition strength were found (Couchman *et al.*, 2010). This suggests that the unitary IPSC - and EPSC strength are regulated specifically in different nuclei of the superior olivary complex in order to fulfill the computational needs of each neuron type. Together with more drastic examples of variations in the synaptic convergence and nerve terminal size like the large, one-to-one connectivity of the excitatory calyces of Held (Forsythe, 1994; Borst *et al.*, 1995), these findings suggest that the strength, and the number of unitary synaptic inputs is specifically adapted to the computations in each neuronal sub-system.

Figure Legends

Figure 1. LSO neurons receive large inhibitory inputs

A1, IPSCs recorded with a high $[Cl^-]_i$ pipette solution, in response to increasing intensities of electrical stimulation. Holding potential was -70 mV. ***A2***, Peak IPSC amplitudes plotted as a function of stimulus intensity. Horizontal lines indicate the average amplitude of each identified step. The arrow indicates fluctuation of IPSC amplitudes evoked under a constant stimulation intensity, indicating that this stimulus intensity was at the threshold for recruiting an additional fiber. N = 8 repetitions at 0.1 Hz for each stimulation intensity. ***A3***, Example traces from the recording in A1 before (in gray) and after offline R_s -compensation (Black or red trace). For the larger IPSC, offline R_s-compensation resulted in a larger than 50 % amplitude increase (red trace, and red data points in A2).The data in A1-A3 are from the same recording. ***B1, B2***, Example IPSC input - output curve from another LSO neuron. In this example, a more gradual IPSC increase was apparent at higher stimulation intensities. ***C***, Histograms of unitary IPSC amplitudes for each recorded cell. Note that for cells #3 and #7, steps could not be identified for all parts of the input-output curve, and the more graded IPSC increase is reported as a dotted line. The example recordings shown in A and B correspond to cells #9 and #7, respectively. ***D***, Histogram of the unitary IPSC amplitudes combined from all recordings (average ± SD: 2.37 ± 2.1 nA; n = 42 unitary IPSCs from n = 9 cells; bin size = 200 pA). Note that the distribution is right-skewed. ***E***, Histogram of all the unitary IPSC amplitudes, logarithmized, and fitted with a Gaussian function. ***F***, Normal probability plot of the logarithmized unitary IPSC amplitudes. Note that the majority of the data points lie close to the unitary line (except for the smallest and largest values), consistent with a normal distribution. ***G***, Plot of the unitary IPSC amplitudes in their order of appearance, from lowest to highest stimulation intensity, for n = 9 recordings. Average values for the first (left) and the last (right) unitary IPSC are also shown (grey average data points ± S.D.)

Figure 2. Inhibitory conductances at physiological intracellular Cl^- concentration

A1, IPSCs recorded with low $[Cl^-]_i$ (6 mM), evoked by increasing electrical stimulation intensities as indicated. Holding potential was -50 mV. ***A2***, Input - output curve for the IPSCs recorded in A1. ***B1***, IPSCs recorded under low $[Cl^-]_i$, at holding potentials ranging of -90 mV, -85 mV and - 80 mV and then increments of + 10 mV. Each trace is the average of n = 8 IPSCs. ***B2***, I-V plots of IPSCs recorded under low $[Cl^-]_i$ conditions (left data points, same recording as in A, B1), and under high $[Cl^-]_i$ from a different cell. ***C***, Reversal potentials obtained for the IPSCs measured under high (n = 2 cells) and low $[Cl^-]_i$ solutions (n = 5 cells). Horizontal bars indicate the average. ***D***, Average and individual values of the conductance of the unitary IPSCs for the data in this Figure measured under low $[Cl^-]_i$ (left). The data on the right represents the conductance values of unitary IPSCs under high $[Cl^-]_i$, converted from the measurements of unitary IPSC shown in Figure 1. Note the significantly smaller unitary IPSCs under conditions of low $[Cl^-]_i$ ($p < 0.0037$; Mann-Whitney test).

Figure 3. Minimal optogenetic stimulation of PV-positive fibers reveals large unitary IPSCs

A, Scheme of the experimental design, in which blue light pulses were delivered onto the LSO (or sometimes MNTB) in PV^{Cre} x *ChR2* mice. ***B***, Immunohistochemistry performed in a PV^{Cre} x *ChR2* mouse at P21on the level of the LSO, with antibodies against VGAT (red channel) and GFP to localize ChR2-eYFP (green channel). Scale bar: 5 µm. ***C1, C2***, Light-evoked IPSCs obtained with 1 ms light pulses onto LSO (blue trace) at increasing light intensities. In ***C2***, the holding potential (V_{hold}) was lowered to -20 mV. ***D***, Plot of the latency of the optogenetically evoked IPSCs as a function of LED light intensity, fitted with a single-exponential function. Data points are from the recording in C. ***E1***, ***E2***, Minimal optogenetic stimulation in the LSO with either 1 ms long pulses (left and middle panel) or with prolonged (5ms) but even dimmer light pulses (right). IPSCs are shown with a continuous line before and with a dotted line after a second peak occurs. ***F***, Histogram of the amplitudes of the first IPSC peaks in ***E***, fitted with a multi-peak Gaussian function (n = 83 events). ***G***, Plot of the unitary IPSC amplitudes for each recorded cell, estimated by optogenetic stimulation in the LSO. For the first five cells, a subsequent optogenetic stimulation was performed in the MNTB (see ***K***). ***H1***, Histogram of the unitary IPSC amplitudes combined from all recordings. ***H2***, Histogram of the logarithmized unitary IPSC amplitudes. The distribution can be fitted with a Gaussian curve, except for the very small values. ***H3***, Normal probability plot of the logarithmized unitary IPSC amplitudes. Note that the majority of the data points lie close to the unitary line, consistent with a log-normal distribution. ***I***, IPSCs recorded in the same neuron as shown in C and E, but with the optical stimulation moved to the MNTB area, for two different light intensities (left, and right). ***J***, Histogram of all the first peak IPSC amplitudes with light stimulation in the MNTB, fitted with a multi-peak Gaussian function (n = 104 events). ***K***, Plot of the unitary IPSC amplitudes for each recorded cell, estimated by optogenetic stimulation in the MNTB. ***L***, Average values of the unitary IPSC amplitudes evoked with light stimulation in the LSO (black) or MNTB (red; n = 45 and 29, respectively). Note the significantly smaller unitary IPSCs evoked by optogenetic stimulation in the MNTB ($p < 0.0005$; Mann-Whitney test). Error bars indicate S.D.

Figure 4. Optogenetic stimulation of the excitatory synapses under the PV promoter reveals small unitary EPSCs amplitudes

A1, Light-evoked EPSCs obtained with 1 ms light pulses to the surrounding LSO tissue at increasing intensities in a PV^{Cre} x *ChR2* mouse. The recordings were done in the presence of strychnine (2 µM) and bicuculline (10 µM) to block inhibitory inputs. The pink trace in the most left graph indicates a failure. The other traces obtained with the same light stimulation were off-set for clarity. Note the early-rising, but more slowly decaying light - evoked photocurrent. Faster rising - and decaying glutamatergic EPSCs are also observed. ***A2***, Input - output curve for the same experiment. Note the discrete, but small first "step" with weak light intensities (see inset). ***B***, Histogram of the EPSC amplitude measured at the threshold for successful stimulation in the same recording as shown in ***A1*** and ***A2***. The average of this distribution (30 ± 15 pA, n = 67 events) was taken as the estimate of the unitary EPSC. ***C***, Individual- and average data points of unitary EPSC amplitudes. Error bars indicate S.D.

Figure 5. Optogenetic stimulation under the Math5 promoter reveals high convergence of bushy cell inputs to LSO neurons

A, Scheme of the experimental design, in which blue light stimulation was delivered to LSO tissue of $Math^{Cre}$ x *ChR2* mice. ***B***, Immunohistochemistry at the level of the LSO with an anti-GFP antibody (green channel, to detect the transgenic ChR2-eYFP), and an anti-VGluT2 antibody (red channel, to detect glutamatergic nerve terminals). Scale bar: 5 µm. ***C***, Light-evoked EPSPs (top traces) and EPSCs (bottom traces) recorded in the same example cell; light stimuli of increasing intensity were applied to the surrounding LSO tissue. ***D1***, Occurrence of APs, and EPSP amplitudes plotted as a function of blue light intensity. A stimulus at a given intensity was repeated three times at 0.1 Hz. ***D2***, EPSC amplitudes plotted as a function of stimulus light intensity. The data in panels ***C - D*** are from the same recording. ***E***, Input-output curves of optically evoked EPSCs for n = 7 cells. Each data point represents the average of n = 3 repeated stimuli at a given light intensity. ***F***, Average- and individual data points of the unitary EPSC amplitude (left), and of the EPSC amplitude measured at the threshold of a reliably triggered AP (right). ***G***, Average- and individual data points of the estimated number of inputs (left), and of the maximal EPSC amplitude (right).

Figure 6. The effective window for inhibition is brief and determined by the ratio of excitatory- and inhibitory conductances

A1, *top*, Response of an LSO neuron to optogenetic stimulation of bushy cell inputs in a *Math5*^{Cre} x *ChR2* mouse at 10% of maximal LED intensity. Note the reliably evoked APs (curtailed at -20 mV). *Bottom*, response of the same LSO neuron to electrical stimulation of MNTB fibers (at 18 V), which generates an IPSP of about - 15 mV, and an IPSC of 0.87 nA (red trace). ***A2***, IPSCs recorded in the same LSO neuron evoked by the two different stimulation intensities (5 and 18 V) used for the E - I integration experiment. ***B***, E - I integration experiment: the timing of optogenetic stimulation (EPSP onset is indicated by a gray arrow) was varied relative to inhibition (indicated with a dashed line) to find the optimal time difference for effective inhibition. The optogenetic stimulation of bushy cell fibers is marked by blue bars (1 ms light pulses at 10 %). The time differences between the onset of the IPSP and the onset of the EPSP are indicated ("Δt" values). Note that AP firing was suppressed (star symbols) when IPSP and EPSP occurred nearly synchronously. ***C***, Probability of AP generation plotted as a function of the time difference between the IPSP and EPSP onset. Red data points were obtained with the higher electrical stimulation intensity (18 V; IPSC of 0.87 nA or 33.5 nS), while the pink data points were obtained with the lower stimulation intensity (5 V; IPSC of 0.31 nA or 12.3 nS). Each data point was estimated from n = 5 repetitions. The width of the inhibition period is referred to as the effective inhibition window. The data in A - C were from the same recording. ***D***, Plot of the effective inhibition window as a function of the inhibitory conductance, for all cells investigated (n = 6). Data points linked by a continuous line represent recordings under the first (usually weaker) optogenetic stimulation of excitatory inputs, whereas data points linked by a dotted line represent recordings with the second (usually stronger) excitatory inputs. The resulting values for excitation strength, g_{exc} (nS), are indicated in the label (value for the second excitation strength, in brackets). ***E***, Same data as in D, but now plotted as a function of the *ratio* between the inhibitory and the excitatory conductance in each cell. The grey area highlights an observed effective inhibition window of 1 – 3 ms, for which ratios of inhibition over excitation of at least 2 were necessary. ***F***, Plot of the IPSC and IPSP half-widths (empty and filled squares, respectively) and of the effective inhibition window (open circles), as a function of G_{inh}.

Figure 7. The strengths and numbers of unitary inhibitory and excitatory inputs are key determinants of the tuning curve and the spontaneous firing properties of LSO neurons

A, Schematic representation of the connectivity of excitatory and inhibitory inputs onto an LSO neuron as modelled here. ***B***, Summary of the parameters used for the model simulations (see Methods for further details). The parameters shown in bold typeset are those of "case 1" (see panels ***D - G***) and these connectivity-related parameters were varied in the simulations; all other parameters were fixed. ***C1***, The simulated firing rates of the excitatory and inhibitory afferents onto an LSO neuron (black and red traces, respectively), which function as input to the model. ***C2***, Plot of the distribution of conductance values of n = 8 inhibitory inputs used for case 1 and 4. ***D1***, Simulated postsynaptic conductances in response to modelled input firing rates of N = 8 inhibitory, and N = 40 excitatory inputs (red and black traces, respectively). ***D2***, The resulting membrane potential (V_m) trace (*top*), spike raster plot for 1000 repetitions (*middle*), and peri-stimulus spike time histograms (*bottom*). Note the large hyperpolarizing fluctuations in the V_m trace caused by the strong unitary strength of inhibition. Inset: distribution of the V_m values under background input activity. ***E1, E2***, Similar display of simulation results as in D1, D2, but now modelled for N = 40 inhibitory afferents, with proportionally reduced unitary IPSC strength (1.8 nS; "case 2"). Note the smaller fluctuations of V_m values (inset), and the absence of spiking responses with the 60 Hz / 60 Hz stimulation, as compared to case 1, and the smaller spontaneous firing visible in the spike raster plots in-between stimulations. ***F***, Average spontaneous firing rates of the LSO neuron for the four modelled cases. ***G***, Evoked firing rates of the LSO neuron for three modelled cases, in response to excitatory inputs firing at 60 Hz and inhibitory inputs firing from 10 to 120 Hz, thus simulating varying sound intensity at the contralateral ear. ***H***, Spontaneous firing rates (*left*) and tuning curve (*right*) when the number of inhibitory inputs is varied over a larger range. ***I***, Spontaneous firing rates (*left*) and tuning curve (*right*) when the number of excitatory inputs is varied over a larger range. Note the strong influence of the excitatory convergence on spontaneous firing rates. ***J***, Evoked firing rates of the LSO neuron for the modelled cases 1 and 4. The error bars in panels ***F* - *I*** correspond to the standard deviation.

Additional information

Competing interests

None declared

Author contribution

The experiments were carried out at the Ecole Polytechnique Fédérale de Lausanne (EPFL), Switzerland. The simulations were done at EPFL (Laboratory of Computational Neuroscience), and at the Centre for Neural Circuits and Behaviour at the University of Oxford. EG and RS designed the project, EG and BB performed the experiments and data analysis, FZ performed the model simulations with inputs from all authors; RS and EG wrote the manuscript. All authors have approved the final version of the manuscript and agree to be accountable for all aspects of the work. All persons designated as authors qualify for authorship and all those who qualify for authorship are listed.

Funding

This work was supported by the Swiss National Science Foundation (National Center of Competence in Research "Synapsy: The Synaptic bases of mental diseases"; to R.S.), by the German Research Foundation (DFG Priority Program 1608 "Ultrafast and temporally precise information processing: Normal and dysfunctional hearing", SCHN 451/5-2; to R.S.), and by a Wellcome Trust fellowship to F.Z. [110124/Z/15/Z].

Acknowledgments

We thank Heather Murray and Jessica Dupasquier for expert technical assistance, Drs. Tim Vogels and Wulfram Gerstner for helpful advice in the initial phase of the modeling, and Drs. Philip Joris, Michael Pecka and Olexiy Kochubey for discussions. Confocal image acquisition was performed in the Bioimaging and optics platform (BIOP) of EPFL.

References:

Ashida G, Tollin DJ & Kretzberg J. (2017). Physiological models of the lateral superior olive. *PLoS computational biology* **13,** e1005903.

Beiderbeck B, Myoga MH, Müller N, I.C., Callan AR, Friauf E, Grothe B & Pecka M. (2018). Precisely timed inhibition facilitates action potential firing for spatial coding in the auditory brainstem. *Nature communications* **9,** 1771.

Bormann J, Hamill OP & Sakmann B. (1987). Mechanism of anion permeation through channels gated by glycine and gamma-aminobutyric acid in mouse cultured spinal neurones. *J Physiol* **385,** 243-286.

Bormann J, Rundstrom N, Betz H & Langosch D. (1993). Residues within transmembrane segment M2 determine chloride conductance of glycine receptor homo- and hetero-oligomers. *The EMBO journal* **12,** 3729-3737.

Borst JG, Helmchen F & Sakmann B. (1995). Pre- and postsynaptic whole-cell recordings in the medial nucleus of the trapezoid body of the rat. *J Physiol* **489 (Pt 3),** 825-840.

Borst JG & Soria van Hoeve J. (2012). The calyx of Held synapse: from model synapse to auditory relay. *Annu Rev Physiol* **74,** 199-224.

Boudreau JC & Tsuchitani C. (1968). Binaural interaction in the cat superior olive S segment. *J Neurophysiol* **31,** 442-454.

Bouhours B, Gjoni E, Kochubey O & Schneggenburger R. (2017). Synaptotagmin2 (Syt2) drives fast release redundantly with Syt1 at the output synapses of Parvalbumin-expressing inhibitory neurons. *J Neurosci* **37,** 4604-4617.

Boyden ES, Zhang F, Bamberg E, Nagel G & Deisseroth K. (2005). Millisecond-timescale, genetically targeted optical control of neural activity. *Nat Neurosci* **8,** 1263-1268.

Caird D & Klinke R. (1983). Processing of binaural stimuli by cat superior olivary complex neurons. *Exp Brain Res* **52,** 385-399.

Cant NB & Benson CG. (2003). Parallel auditory pathways: projection patterns of the different neuronal populations in the dorsal and ventral cochlear nuclei. *Brain Res Bull* **60,** 457-474.

Case DT & Gillespie DC. (2011). Pre- and postsynaptic properties of glutamatergic transmission in the immature inhibitory MNTB-LSO pathway. *J Neurophysiol* **106,** 2570-2579.

Case DT, Zhao X & Gillespie DC. (2011). Functional refinement in the projection from ventral cochlear nucleus to lateral superior olive precedes hearing onset in rat. *PLoS One* **6,** e20756.

Clause A, Kim G, Sonntag M, Weisz CJ, Vetter DE, Rübsamen R & Kandler K. (2014). The precise temporal pattern of prehearing spontaneous activity is necessary for tonotopic map refinement. *Neuron* **82,** 822-835.

Couchman K, Grothe B & Felmy F. (2010). Medial superior olivary neurons receive surprisingly few excitatory and inhibitory inputs with balanced strength and short-term dynamics. *J Neurosci* **30,** 17111-17121.

Denk W & Horstmann H. (2004). Serial block-face scanning electron microscopy to reconstruct three-dimensional tissue nanostructure. *PLoS Biol* **2,** e329.

Ehrlich I, Löhrke S & Friauf E. (1999). Shift from depolarizing to hyperpolarizing glycine action in rat auditory neurones is due to age-dependent Cl- regulation. *J Physiol* **520 Pt 1,** 121-137.

Fatt P & Katz B. (1953). The effect of inhibitory nerve impulses on a crustacean muscle fibre. *J Physiol* **121,** 374-389.

Felix RA, 2nd & Magnusson AK. (2016). Development of excitatory synaptic transmission to the superior paraolivary and lateral superior olivary nuclei optimizes differential decoding strategies. *Neuroscience* **334,** 1-12.

Felmy F & Schneggenburger R. (2004). Developmental expression of the Ca^{2+}-binding proteins calretinin and parvalbumin at the calyx of Held of rats and mice. *Eur J Neurosci* **20,** 1473-1482.

Filliben JJ. (1975). The probability plot correlation coefficient test for normality. *Technometrics* **17,** 111-117.

Forsythe ID. (1994). Direct patch recording from identified presynaptic terminals mediating glutamatergic EPSCs in the rat CNS, *in vitro*. *J Physiol* **479,** 381-387.

Friauf E, Hammerschmidt B & Kirsch J. (1997). Development of adult-type inhibitory glycine receptors in the central auditory system of rats. *J Comp Neurol* **385,** 117-134.

Gerstner W, Kistler WM, Naud R & Paninski L. (2014). Neuronal dynamics: from single neurons to networks and models of cognition. *Cambridge University Press* **Cambridge**.

Gillespie DC, Kim G & Kandler K. (2005). Inhibitory synapses in the developing auditory system are glutamatergic. *Nat Neurosci* **8,** 332-338.

Gjoni E, Aguet C, Sahlender DA, Knott G & Schneggenburger R. (accompanying manuscript). Ultrastructural basis of strong unitary inhibition in a binaural neuron. *co-submitted to J Physiology*.

Grothe B, Pecka M & McAlpine D. (2010). Mechanisms of sound localization in mammals. *Physiol Rev* **90,** 983-1012.

Hippenmeyer S, Vrieseling E, Sigrist M, Portmann T, Laengle C, Ladle DR & Arber S. (2005). A developmental switch in the response of DRG neurons to ETS transcription factor signaling. *PLoS Biol* **3,** e159.

Hirtz JJ, Braun N, Griesemer D, Hannes C, Janz K, Lohrke S, Müller B & Friauf E. (2012). Synaptic refinement of an inhibitory topographic map in the auditory brainstem requires functional Cav1.3 calcium channels. *J Neurosci* **32,** 14602-14616.

Hruskova B, Trojanova J, Kulik A, Kralikova M, Pysanenko K, Bures Z, Syka J, Trussell LO & Turecek R. (2012). Differential distribution of glycine receptor subtypes at the rat calyx of Held synapse. *J Neurosci* **32,** 17012-17024.

Jalabi W, Kopp-Scheinpflug C, Allen PD, Schiavon E, DiGiacomo RR, Forsythe ID & Maricich SM. (2013). Sound localization ability and glycinergic innervation of the superior olivary complex persist after genetic deletion of the medial nucleus of the trapezoid body. *J Neurosci* **33,** 15044-15049.

Karcz A, Hennig MH, Robbins CA, Tempel BL, Rübsamen R & Kopp-Scheinpflug C. (2011). Low-voltage activated Kv1.1 subunits are crucial for the processing of sound source location in the lateral superior olive in mice. *J Physiol* **589,** 1143-1157.

Kim G & Kandler K. (2003). Elimination and strengthening of glycinergic/GABAergic connections during tonotopic map formation. *Nat Neurosci* **6,** 282-290.

Kim G & Kandler K. (2010). Synaptic changes underlying the strengthening of GABA/glycinergic connections in the developing lateral superior olive. *Neuroscience* **171,** 924-933.

Koch U, Braun M, Kapfer C & Grothe B. (2004). Distribution of HCN1 and HCN2 in rat auditory brainstem nuclei. *Eur J Neurosci* **20,** 79-91.

Kopp-Scheinpflug C, Fuchs K, Lippe WR, Tempel BL & Rübsamen R. (2003). Decreased temporal precision of auditory signaling in Kcna1-null mice: an electrophysiological study in vivo. *J Neuroscience* **23,** 9199-9207.

Kopp-Scheinpflug C, Tozer AJ, Robinson SW, Tempel BL, Hennig MH & Forsythe ID. (2011). The sound of silence: ionic mechanisms encoding sound termination. *Neuron* **71,** 911-925.

Kotak VC, Korada S, Schwartz IR & Sanes DH. (1998). A developmental shift from GABAergic to glycinergic transmission in the central auditory system. *J Neuroscience* **18,** 4646-4655.

Kronander E, Michalski N, Lebrand C, Hornung JP & Schneggenburger R. (2017). An organotypic slice culture to study the formation of calyx of Held synapses in-vitro. *PLoS One* **12,** e0175964.

Leao KE, Leao RN & Walmsley B. (2011). Modulation of dendritic synaptic processing in the lateral superior olive by hyperpolarization-activated currents. *Eur J Neurosci* **33,** 1462-1470.

Liberman MC. (1978). Auditory-nerve response from cats raised in a low-noise chamber. *J Acoust Soc Am* **63,** 442-455.

Litvina EY & Chen C. (2017). Functional convergence at the retinogeniculate synapse. *Neuron* **96,** 330-338 e335.

Lohmann C & Friauf E. (1996). Distribution of the calcium-binding proteins parvalbumin and calretinin in the auditory brainstem of adult and developing rats. *J Comp Neurol* **367,** 90-109.

Lu HW & Trussell LO. (2016). Spontaneous activity defines effective convergence ratios in an inhibitory circuit. *J Neuroscience* **36,** 3268-3280.

Madisen L, Mao T, Koch H, Zhuo JM, Berenyi A, Fujisawa S, Hsu YW, Garcia AJ, 3rd, Gu X, Zanella S, Kidney J, Gu H, Mao Y, Hooks BM, Boyden ES, Buzsaki G, Ramirez JM, Jones AR, Svoboda K, Han X, Turner EE & Zeng H. (2012). A toolbox of Cre-dependent optogenetic transgenic mice for light-induced activation and silencing. *Nat Neurosci* **15,** 793-802.

Magnusson AK, Park TJ, Pecka M, Grothe B & Koch U. (2008). Retrograde GABA signaling adjusts sound localization by balancing excitation and inhibition in the brainstem. *Neuron* **59,** 125-137.

Masterton B, Jane JA & Diamond IT. (1967). Role of brainstem auditory structures in sound localization. I. Trapezoid body, superior olive, and lateral lemniscus. *J Neurophysiol* **30,** 341-359.

Meier J & Schmieden V. (2003). Inhibition of alpha-subunit glycine receptors by quinoxalines. *Neuroreport* **14,** 1507-1510.

Meyer AC, Neher E & Schneggenburger R. (2001). Estimation of quantal size and number of functional active zones at the calyx of Held synapse by nonstationary EPSC variance analysis. *J Neuroscience* **21,** 7889-7900.

Noh J, Seal RP, Garver JA, Edwards RH & Kandler K. (2010). Glutamate co-release at GABA/glycinergic synapses is crucial for the refinement of an inhibitory map. *Nat Neurosci* **13,** 232-238.

Petreanu L, Huber D, Sobczyk A & Svoboda K. (2007). Channelrhodopsin-2-assisted circuit mapping of long-range callosal projections. *Nat Neurosci* **10,** 663-668.

Pfeiffer RR. (1966). Classification of response patterns of spike discharges for units in the cochlear nucleus: tone-burst stimulation. *Exp Brain Res* **1,** 220-235.

Pilati N, Linley DM, Selvaskandan H, Uchitel O, Hennig MH, Kopp-Scheinpflug C & Forsythe ID. (2016). Acoustic trauma slows AMPA receptor-mediated EPSCs in the auditory brainstem, reducing GluA4 subunit expression as a mechanism to rescue binaural function. *J Physiol* **594,** 3683-3703.

Reed MC & Blum JJ. (1990). A model for the computation and encoding of azimuthal information by the lateral superior olive. *J Acoust Soc Am* **88,** 1442-1453.

Sanes DH. (1990). An in vitro analysis of sound localization mechanisms in the gerbil lateral superior olive. *J Neurosci* **10,** 3494-3506.

Sanes DH & Takacs C. (1993). Activity-dependent refinement of inhibitory connections. *Eur J Neurosci* **5,** 570-574.

Saul SM, Brzezinski JA, Altschuler RA, Shore SE, Rudolph DD, Kabara LL, Halsey KE, Hufnagel RB, Zhou J, Dolan DF & Glaser T. (2008). Math5 expression and function in the central auditory system. *Mol Cell Neurosci* **37,** 153-169.

Schneggenburger R & Forsythe ID. (2006). The calyx of Held. *Cell Tissue Res* **326,** 311-337.

Smith PH, Joris PX, Carney LH & Yin TCT. (1991). Projections of physiologically characterized globular bushy cell axons from the cochlear nucleus of the cat. *J Comp Neurol* **304,** 387-407.

Smith PH, Joris PX & Yin TC. (1993). Projections of physiologically characterized spherical bushy cell axons from the cochlear nucleus of the cat: evidence for delay lines to the medial superior olive. *J Comp Neurol* **331,** 245-260.

Smith PH, Joris PX & Yin TC. (1998). Anatomy and physiology of principal cells of the medial nucleus of the trapezoid body (MNTB) of the cat. *Journal of Neurophysiology* **79,** 3127-3142.

Spirou GA, Brownell WE & Zidnac M. (1990). Recordings from cat trapezoid body and HRP labeling of globular bushy cell axons. *J Neurophysiol* **63,** 1169-1190.

Sterenborg JC, Pilati N, Sheridan CJ, Uchitel OD, Forsythe ID & Barnes-Davies M. (2010). Lateral olivocochlear (LOC) neurons of the mouse LSO receive excitatory and inhibitory synaptic inputs with slower kinetics than LSO principal neurons. *Hear Res* **270,** 119-126.

Tollin DJ. (2003). The lateral superior olive: a functional role in sound source localization. *The Neuroscientist : a review journal bringing neurobiology, neurology and psychiatry* **9,** 127-143.

Tsuchitani C & Boudreau JC. (1966). Single unit analysis of cat superior olive S segment with tonal stimuli. *Journal of Neurophysiology* **29,** 684-697.

von Gersdorff H, Schneggenburger R, Weis S & Neher E. (1997). Presynaptic depression at a calyx synapse: The small contribution of metabotropic glutamate receptors. *J Neurosci* **17,** 8137-8146.

Walcher J, Hassfurth B, Grothe B & Koch U. (2011). Comparative posthearing development of inhibitory inputs to the lateral superior olive in gerbils and mice. *J Neurophysiol* **106,** 1443-1453.

Wu SH & Kelly JB. (1992). Binaural interaction in the lateral superior olive: time difference sensitivity studied in mouse brain slice. *J Neurophysiol* **68,** 1151-1159.

Xiao L, Han Y, Runne H, Murray H, Kochubey O, Luthi-Carter R & Schneggenburger R. (2010). Developmental expression of Synaptotagmin isoforms in single calyx of Held - generating neurons. *Mol Cell Neurosci* **44,** 374-385.

Xiao L, Michalski N, Kronander E, Gjoni E, Genoud C, Knott G & Schneggenburger R. (2013). BMP signaling specifies the development of a large and fast CNS synapse. *Nat Neurosci* **16,** 856-864.

Yang Z, Ding K, Pan L, Deng M & Gan L. (2003). Math5 determines the competence state of retinal ganglion cell progenitors. *Developmental biology* **264,** 240-254.

Zenke F & Gerstner W. (2014). Limits to high-speed simulations of spiking neural networks using general-purpose computers. *Frontiers in neuroinformatics* **8,** 76.

Zhang YP & Oertner TG. (2007). Optical induction of synaptic plasticity using a light-sensitive channel. *Nat Methods* **4,** 139-141.

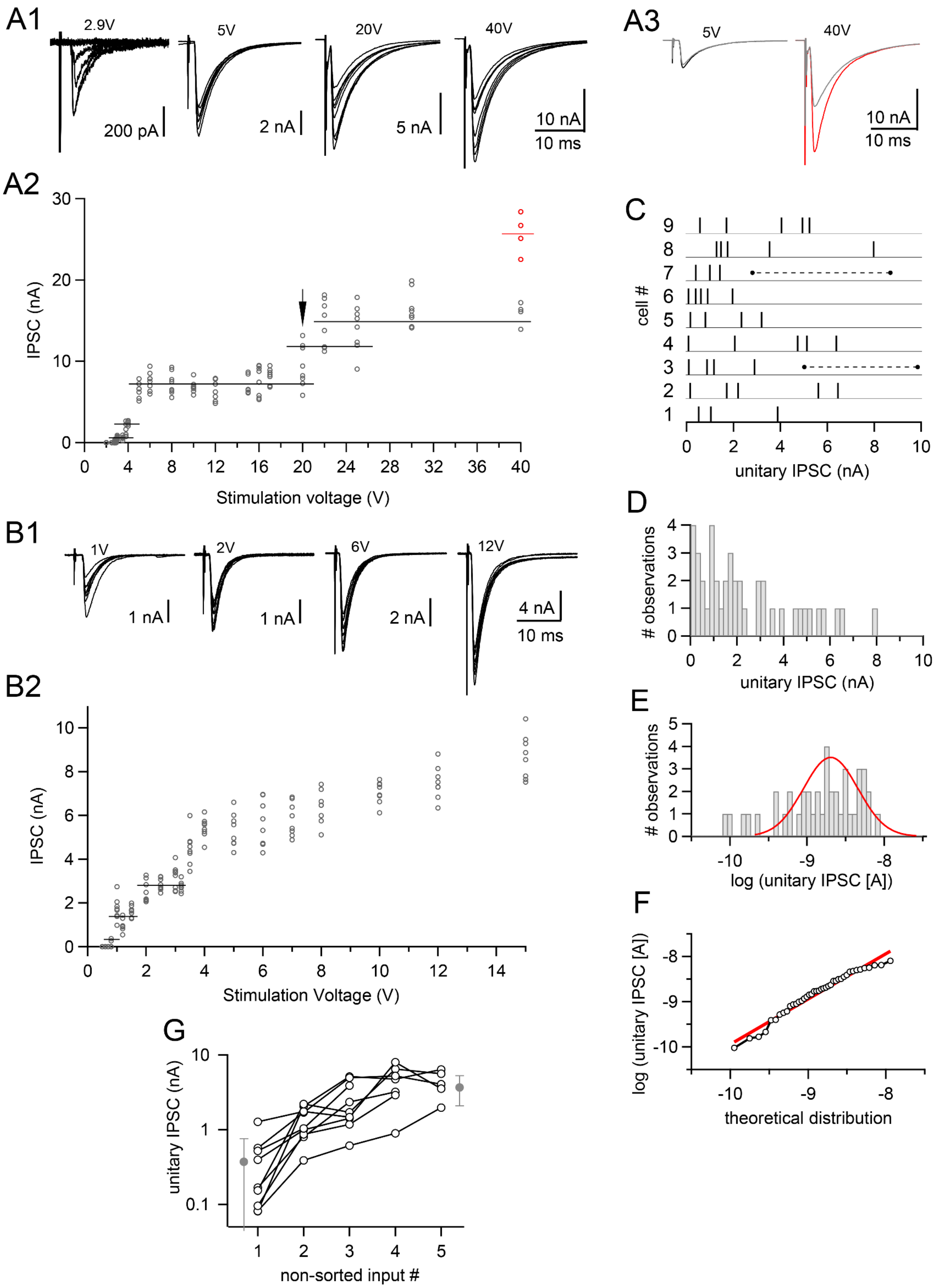
A1
2.9V
5V
20V
40V
200 pA
2 nA
5 nA
10 nA
10 ms
A3
5V
40V
10 nA
10 ms
A2
30
20
10
0
IPSC (nA)
0 4 8 12 16 20 24 28 32 36 40
Stimulation voltage (V)
C
9 8 7 6 5 4 3 2 1
cell #
0 2 4 6 8 10
unitary IPSC (nA)
D
4 3 2 1 0
observations
0 2 4 6 8 10
unitary IPSC (nA)
B1
1V
2V
6V
12V
1 nA
1 nA
2 nA
4 nA
10 ms
B2
10 8 6 4 2 0
IPSC (nA)
0 2 4 6 8 10 12 14
Stimulation Voltage (V)
E
5 4 3 2 1 0
observations
-10 -9 -8
log (unitary IPSC [A])
F
-8 -9 -10
log (unitary IPSC [A])
-10 -9 -8
theoretical distribution
G
10 1 0.1
unitary IPSC (nA)
1 2 3 4 5
non-sorted input #

Figure 1

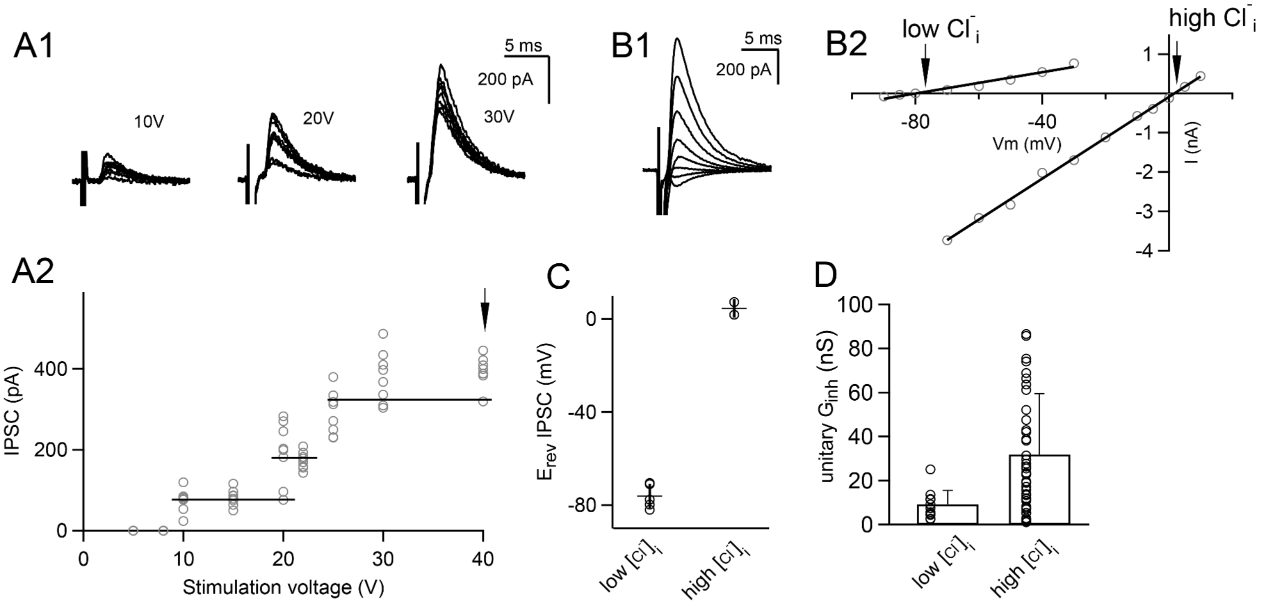
A1
5 ms
200 pA
10V
20V
30V
B1
5 ms
200 pA
B2
low Cl^-_i
high Cl^-_i
1
-80
-40
Vm (mV)
-1
-2
-3
-4
I (nA)
A2
IPSC (pA)
0
200
400
0
10
20
30
40
Stimulation voltage (V)
C
E$_{rev}$ IPSC (mV)
0
-40
-80
low [Cl$^-$]$_i$
high [Cl$^-$]$_i$
D
unitary G$_{inh}$ (nS)
100
80
60
40
20
0
low [Cl$^-$]$_i$
high [Cl$^-$]$_i$

Figure 2

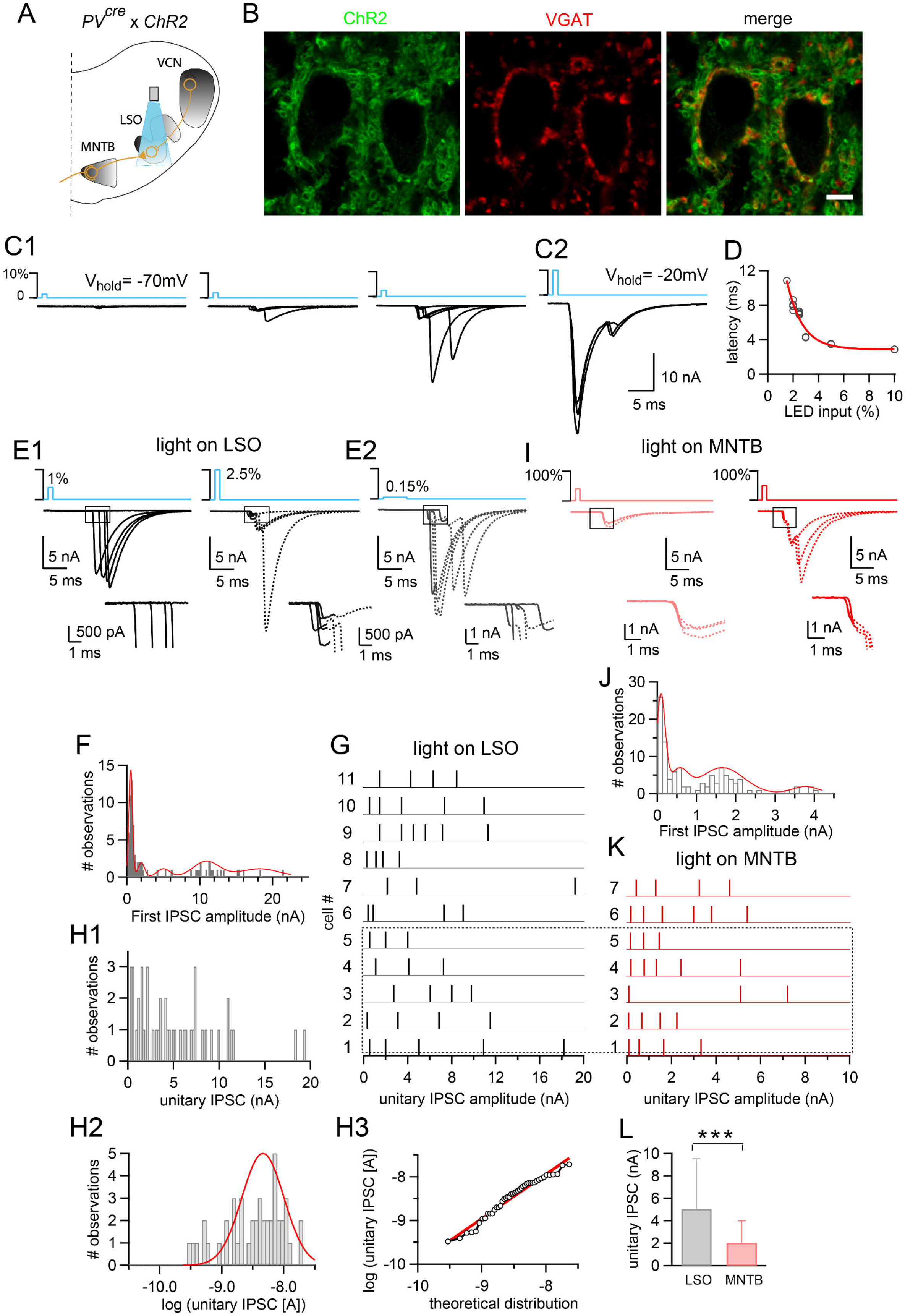
A
PV^{cre} x ChR2
VCN
LSO
MNTB
B
ChR2
VGAT
merge
C1
10%
0
V_{hold}= -70mV
C2
V_{hold}= -20mV
10 nA
5 ms
D
latency (ms)
LED input (%)
E1
light on LSO
1%
2.5%
5 nA
5 ms
500 pA
1 ms
E2
0.15%
1 nA
I
light on MNTB
100%
F
observations
First IPSC amplitude (nA)
G
light on LSO
cell #
unitary IPSC amplitude (nA)
J
observations
First IPSC amplitude (nA)
K
light on MNTB
unitary IPSC amplitude (nA)
H1
observations
unitary IPSC (nA)
H2
observations
log (unitary IPSC [A])
H3
log (unitary IPSC [A])
theoretical distribution
L
unitary IPSC (nA)
***
LSO
MNTB

Figure 3

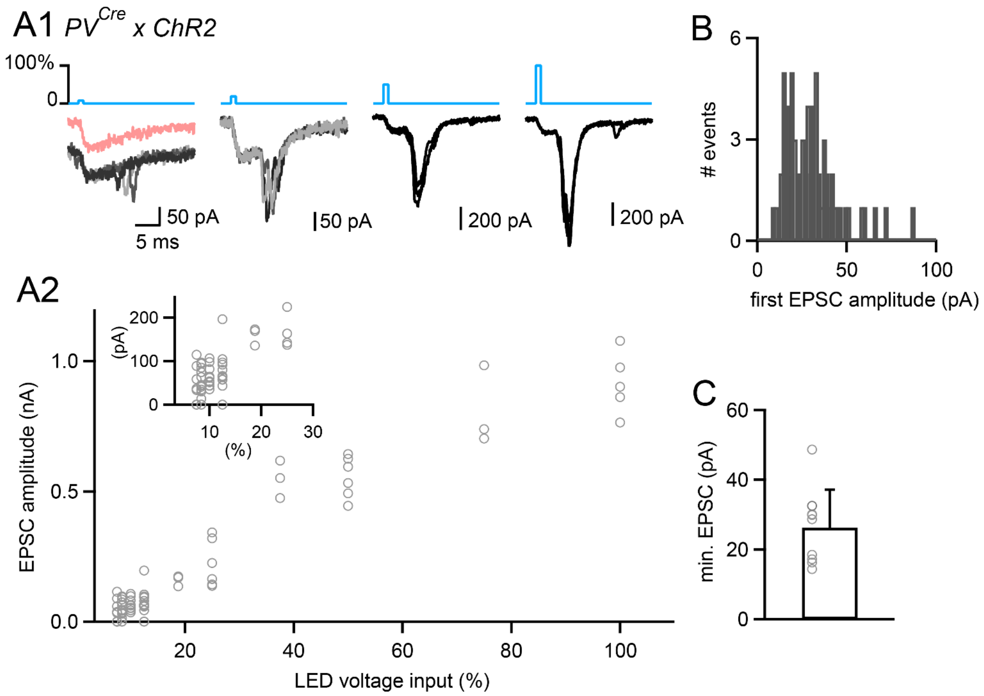
A1 PVCre x ChR2
100%
0
50 pA
5 ms
50 pA
200 pA
200 pA
B
6
3
0
events
0
50
100
first EPSC amplitude (pA)
A2
EPSC amplitude (nA)
1.0
0.5
0.0
20
40
60
80
100
LED voltage input (%)
(pA)
200
100
0
10
20
30
(%)
C
60
40
20
0
min. EPSC (pA)

Figure 4

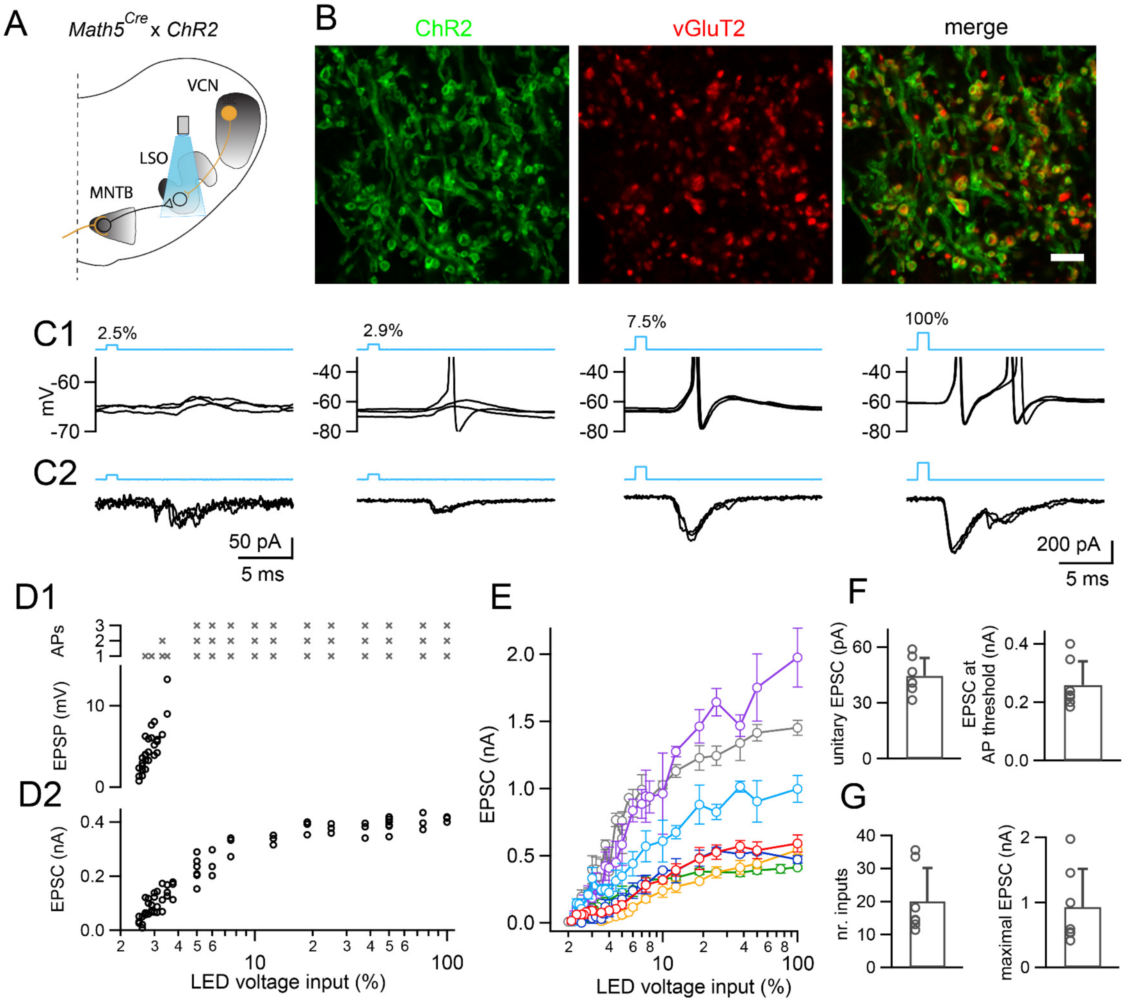
A
Math5^Cre x ChR2
VCN
LSO
MNTB
B
ChR2
vGluT2
merge
C1
2.5%
2.9%
7.5%
100%
mV
-60
-70
-40
-60
-80
C2
50 pA
5 ms
200 pA
5 ms
D1
APs
3
2
1
EPSP (mV)
10
0
D2
EPSC (nA)
0.4
0.2
0.0
2 3 4 5 6 10 2 3 4 5 6 100
LED voltage input (%)
E
EPSC (nA)
2.0
1.5
1.0
0.5
0.0
2 4 6 8 10 2 4 6 8 100
LED voltage input (%)
F
unitary EPSC (pA)
60
30
0
EPSC at AP threshold (nA)
0.4
0.2
0.0
G
nr. inputs
40
30
20
10
0
maximal EPSC (nA)
2
1
0

Figure 5

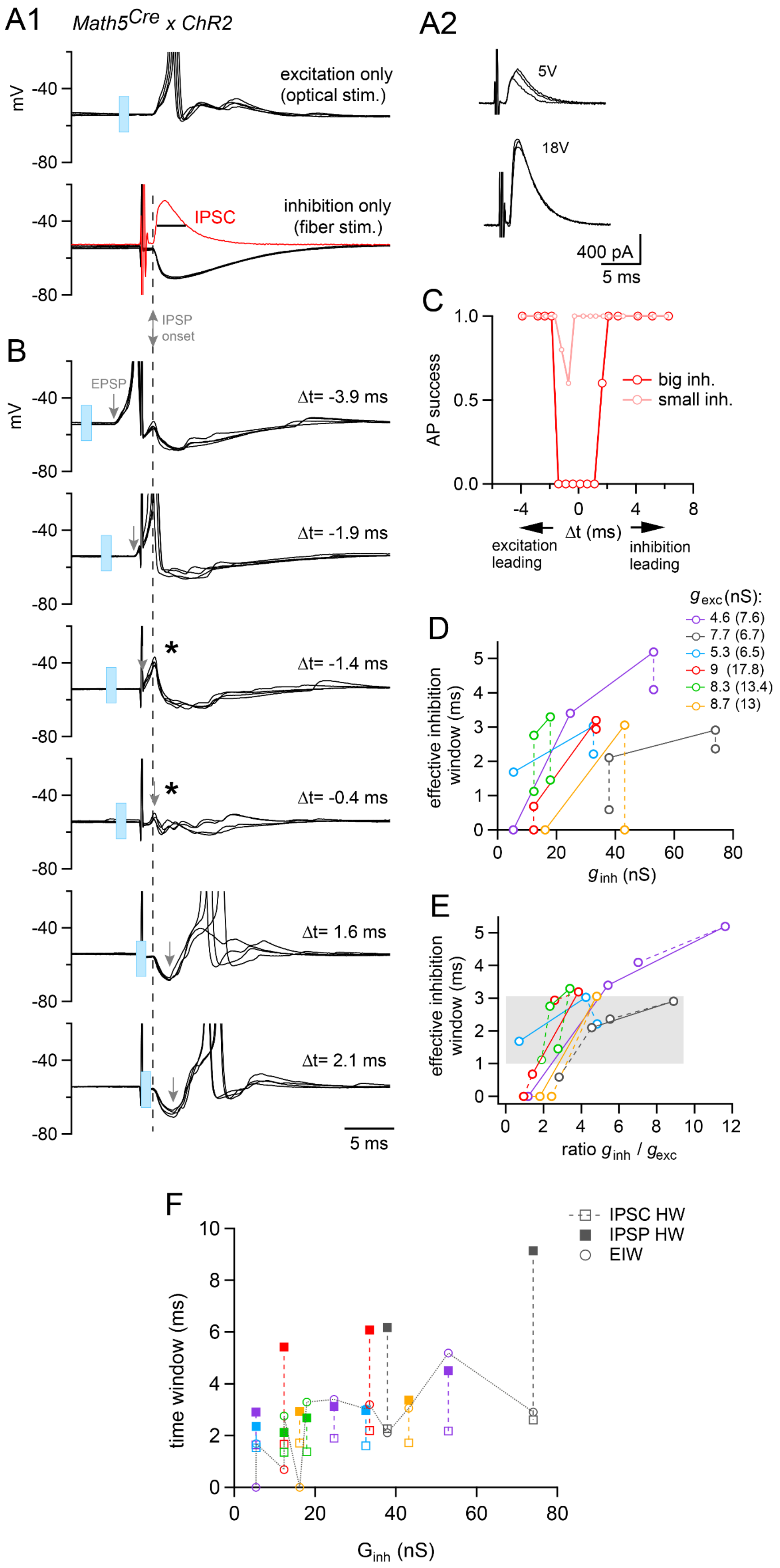
A1
Math5Cre x ChR2
mV
-40
-80
excitation only
(optical stim.)
-40
-80
IPSC
inhibition only
(fiber stim.)
IPSP
onset
A2
5V
18V
400 pA
5 ms
B
EPSP
mV
-40
-80
Δt= -3.9 ms
Δt= -1.9 ms
Δt= -1.4 ms
*
Δt= -0.4 ms
*
Δt= 1.6 ms
Δt= 2.1 ms
5 ms
C
AP success
1.0
0.5
0.0
big inh.
small inh.
-4
0
4
8
Δt (ms)
excitation
leading
inhibition
leading
D
gexc (nS):
4.6 (7.6)
7.7 (6.7)
5.3 (6.5)
9 (17.8)
8.3 (13.4)
8.7 (13)
effective inhibition
window (ms)
0
1
2
3
4
5
0
20
40
60
80
ginh (nS)
E
effective inhibition
window (ms)
0
2
4
6
8
10
12
ratio ginh / gexc
F
IPSC HW
IPSP HW
EIW
time window (ms)
0
2
4
6
8
10
0
20
40
60
80
Ginh (nS)

Figure 6

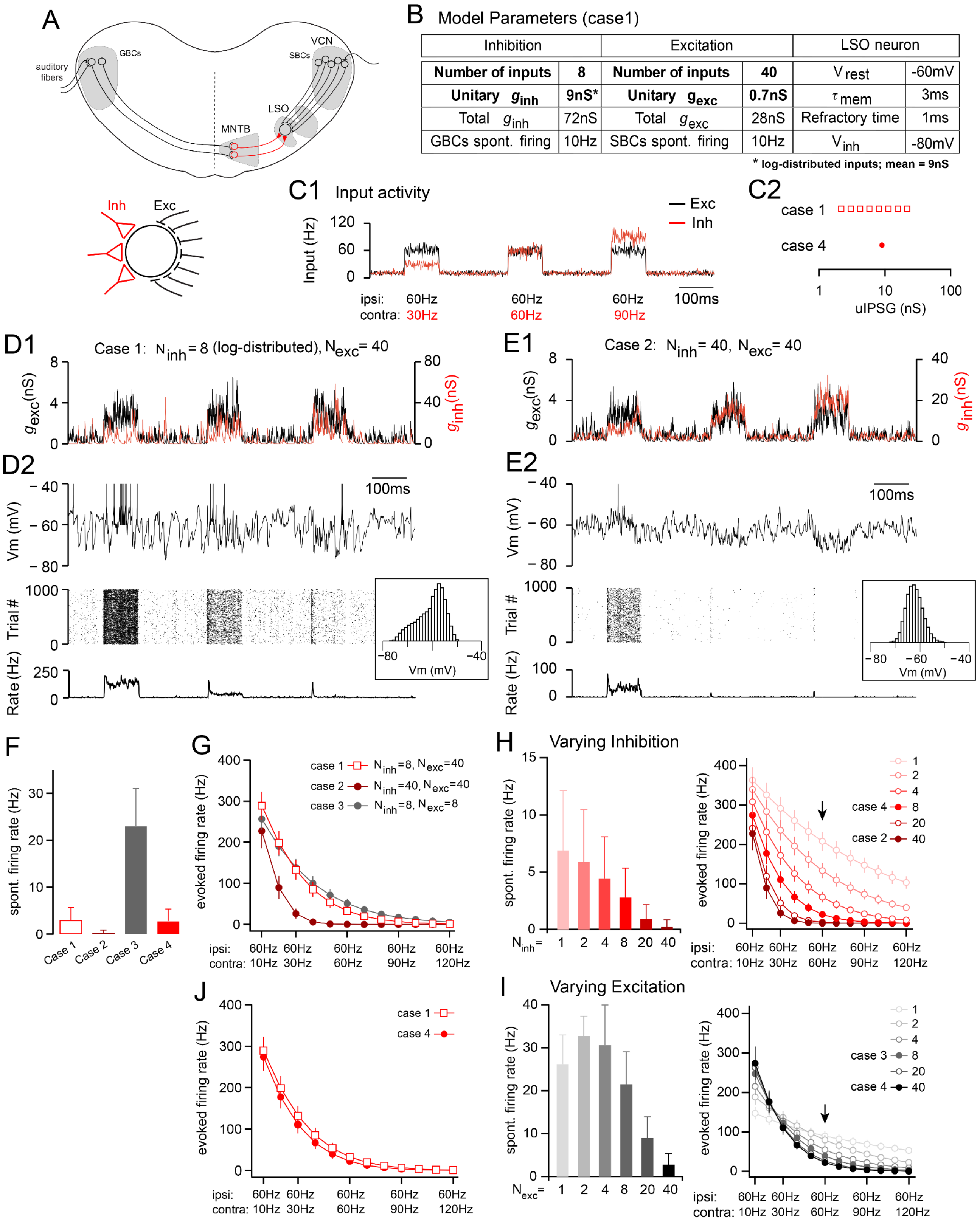

Inhibition		Excitation		LSO neuron	
Number of inputs	**8**	**Number of inputs**	**40**	V_{rest}	-60mV
Unitary g_{inh}	**9nS***	**Unitary g_{exc}**	**0.7nS**	τ_{mem}	3ms
Total g_{inh}	72nS	Total g_{exc}	28nS	Refractory time	1ms
GBCs spont. firing	10Hz	SBCs spont. firing	10Hz	V_{inh}	-80mV

*** log-distributed inputs; mean = 9nS**

Figure 7